JPhys Energy

PURPOSE-LED PUBLISHING™

PAPER • OPEN ACCESS

Structural, optoelectronic and magnetic characterization of Cu_2MnSnS_4 thin films and correlation with photovoltaic performances

To cite this article: Fabio Butrichi *et al* 2026 *J. Phys. Energy* **8** 015022

Journal of Physics: Energy

OPEN ACCESS

RECEIVED
3 July 2025

REVISED
26 January 2026

ACCEPTED FOR PUBLICATION
6 February 2026

PUBLISHED
19 February 2026

PAPER

Structural, optoelectronic and magnetic characterization of Cu_2MnSnS_4 thin films and correlation with photovoltaic performances

Fabio Butrichi[1,2,*], **Giorgio Tseberlidis**[1,3], **Vanira Trifiletti**[1,*], **Davide Delmonte**[4], **Matteo Bronzoni**[4], **René Schwiddessen**[5], **Galina Gurieva**[5], **Marin Rusu**[5], **Simona Binetti**[1] and **Susan Schorr**[5,6]

[1] Department of Materials Science and Solar Energy Research Center (MIB-SOLAR), University of Milano-Bicocca, 20125 Milano, Italy
[2] Department of Information and Electrical Engineering and Applied Mathematics (DIEM), University of Salerno, Via Giovanni Paolo II, Fisciano, SA, Italy
[3] Institute of Science, Technology and Sustainability for Development of Ceramic Materials, National Research Council, 48018 Faenza , RA, Italy
[4] Institute of Materials for Electronics and Magnetism—CNR, Parco Area delle Scienze 37/A, 43124 Parma, Italy
[5] Helmholtz-Zentrum Berlin für Materialien und Energie, Berlin, Germany
[6] Institut für Geologische Wissenschaften, Freie Universität Berlin, Berlin, Germany
[*] Authors to whom any correspondence should be addressed.

E-mail: vanira.trifiletti@unimib.it and fabio.butrichi@unimib.it

Keywords: Earth-abundant photovoltaics, stannite, manganese, grazing incidence, defects, transport properties, magnetic properties

Supplementary material for this article is available online

Abstract

Cu_2MnSnS_4 (CMTS) is regarded as an emerging absorber for thin-film photovoltaic (PV) devices. In this work, CMTS thin films prepared using a low-cost, straightforward solution-based technique were extensively characterized, and the results were correlated with the preparation conditions and corresponding PV performances. X-ray diffraction techniques have been used to study crystallographic structure and microstructural parameters, while energetic band positions were depicted exploiting photoelectron yield spectroscopy and Kelvin probe measurements. The importance of fine-tuning the composition of the starting solution and the beneficial effect of post-deposition treatments were consequently highlighted. A strategy of slow cooling after annealing was studied, resulting in a new record for wet-prepared CMTS, with a champion device yielding 0.97% efficiency 5 months after the first PV measurement. Factors responsible for the typical modest efficiencies of CMTS have been investigated: photoluminescence revealed the presence of intra-gap defects, magnetic characterization revealed room-temperature short-range magnetic ordering, and electrical transport and thermal measurements highlighted a semimetallic-like character, all of which are barriers to achieving high PV performance in CMTS-based devices. Moreover, magnetometry indicates a weakly ordered spin-glass-like state, providing insight into the electronic correlations underlying the observed transport behavior.

1. Introduction

In recent years, renewable energy research has focused particularly on the development of thin-film photovoltaic (PV) technologies, which require less active material and exhibit very high light absorption coefficients [1]. They are lightweight and can be prepared on flexible substrates [2], with potential for use in PV integration in buildings or portable electronic devices. Chalcogenide semiconductors can be used as absorbers in thin-film PV; CdTe and Cu(In, Ga)Se_2 (CIGS) have been widely studied and have achieved efficiencies comparable to those of silicon [3, 4]. Still, their large-scale application is limited since they rely on critical raw materials, such as indium, gallium, and tellurium [5]. Recently, Sb_2Se_3 has

also attracted the attention of researchers due to its remarkable stability and ease of synthesis at a low cost [6, 7]. Currently, the efficiency record is around 10%; further improving the properties and efficiency of Sb_2Se_3-based devices still depends on resolving some open issues, such as passivation, surface treatments, and post-deposition processes (both chemical and thermal) [8]. Besides, $Cu_2ZnSn(S, Se)_4$ (CZTSSe), with kesterite-type structure (space group $I\bar{4}$) [9], is made of cost-effective, eco-friendly, and abundant elements [10, 11], has a high absorption coefficient of 10^4 cm^{-1} [12] and a tunable band-gap (E_g) along the visible range of light, by varying the ratio of the anions [13] spanning from 1.0 eV to 1.5 eV. The reported record efficiency for CZTSSe is 15.9% [14]; the main issue still to be solved resides in the large V_{OC} deficit. The substitution, partial or total, of one or more cations with an isoelectronic cation enables the preparation of CZTSSe alloys with different structural and electronic properties and enhanced PV performance. For instance, Cu^+ can be partially substituted by the isovalent Ag^+ cation, yielding $(Ag, Cu)_2ZnSn(S, Se)_4$ (ACZTSSe). Ag^+ shows a much bigger ionic radius (1.14 Å) [15] than Cu^+ and Zn^{2+} (0.74 Å) [15]: as a consequence, the formation of anti-site defects is reduced [16] and tailing of the valence band related to antisites [17] is mitigated. Substituting Sn atoms with smaller Ge atoms widens the band gap. By increasing the ratio of Ge with respect to Sn (Ge/(Ge + Sn) ratio), E_g increases almost linearly [18], reaching 1.43 eV for pure $Cu_2ZnGeSe_4$ [19] and 2.25 eV for pure Cu_2ZnGeS_4 [20]. An exciting possibility is substituting zinc with more abundant elements. As an example, iron can substitute zinc, forming $Cu_2(Zn, Fe)Sn(S, Se)_4$ in which E_g is tunable by the variation of the iron/zinc ratio [21]. The record efficiency (η) for Cu_2FeSnS_4 is 2.93% [22]. A promising alternative to zinc substitution is manganese, which it is safer and more Earth-abundant than zinc [23]. In particular, the pure sulfide Cu_2MnSnS_4 (CMTS) is a material with the stannite structure and a high absorption coefficient (beyond 10^4 cm^{-1}) [24]; the optical band gap has been reported to vary from 1.1 eV to 1.6 eV [25] depending on the preparation technique. However, it can be tuned to approximately 1.5 eV, the optimal value for achieving the highest theoretical efficiency [17]. Many simulation studies have predicted high efficiencies for CMTS-based devices, reaching or even exceeding those of CZTSSe [26, 27]. Nevertheless, the reported device efficiencies are still low. CMTS can be prepared both through physical and chemical methods. Some of the present authors reported on the physical deposition of CMTS via sulfurization of evaporated metals [28], achieving a modest $\eta = 0.33\%$, mainly due to an insulating secondary phase. In another work, they demonstrated the beneficial effect of both a copper-poor composition and a high-temperature treatment of the device, reaching $\eta = 0.83\%$ [29]. Indeed, solution methods have also been studied, as they reduce processing costs and eliminate the need for vacuum use. The spin-coating deposition of CMTS solution dates back to the publication by Chen and co-workers [24], which first demonstrated the CMTS potential as a PV absorber, achieving $\eta = 0.49\%$. Prabhakar and co-workers improved the efficiency to 0.73% through spray pyrolysis of a solution containing all precursors and sodium as a dopant [30]. Yu *et al* reported CMTS preparation by electrodeposition of precursors in solution with $\eta = 0.76\%$ [31], which was further increased to 0.91% with fine-tuning of the deposition temperature at 560 °C [32]. More recently, some of the present authors reported CMTS synthesis via sulfurization of sputtered precursors; the initial efficiency was 0.65%, but after 1 year of aging, it reached $\eta = 1.13\%$, establishing the current record efficiency for CMTS [33]. The beneficial effects of a Cu-poor composition and the device's high-temperature treatment were confirmed; moreover, the importance of HCl etching on the CMTS surface was reported for the first time. The main limitation was the manganese oxidation process, leading to detrimental secondary phases of MnO_x. These phases act as recombination centers, creating non-radiative recombination pathways, and their semiconductive or insulating nature can severely impact the overall efficiency [33, 34]. Today, the highest efficiency for CMTS prepared from the solution was reported in a previous work conducted by some of the present authors [35]. CMTS thin films were prepared by blade-coating of the substrate with a solution containing all the precursors, followed by annealing at 550 °C, without the need for external sulfurizing agents. The preparation was optimized, leading to pure CMTS without any oxidized forms of manganese, and the importance of HCl etching, thermal treatment (TT) of the device, and the aging previously reported [33] was confirmed. Nevertheless, efficiency never exceeded 0.92%; this was mainly attributed to the use of CdS as an n-type buffer layer [35]. The band alignment was found to be cliff-like, which enhances the risk of recombination. Additionally, a loss of manganese from the surface during CdS deposition was observed, highlighting the need for alternative buffer layers to replace the toxic CdS [13, 35–37]. In addition to the proven poor quality of the interfaces with the charge extractors, the reported PV performances are very low.

Another important factor reducing the efficiency could be related to the charge transport and magnetic properties of CMTS. A very high charge carrier density, in the order of 10^{19} cm^{-3}[30] or 10^{20} cm^{-3} [38], which could increase the metallic character and reduce the shunt resistance and the

collection efficiency, was observed in CMTS; moreover, the resistivity of CMTS thin film at room temperature was found to be low (between 1 Ω·cm and 3 Ω·cm) [39], confirming the possible partial metallic character of this material. As the Mn^{2+} ion possesses five unpaired electrons in the valence shell, many authors theoretically proposed the existence of magnetic properties in CMTS [40, 41]; subsequently, an order dynamic of a different nature based on preparation conditions was experimentally found [38, 42, 43]. It is worth noting that the magnetic properties should be considered in PV applications, as the spin interactions could offer a path for carrier recombination [44, 45].

Therefore, here, the crystallographic and electronic structure of CMTS thin films, prepared with the same methodology, have been extensively studied by referencing highly crystalline systems, such as thin films produced via sputtering [33], single crystals [42, 46, 47], and polycrystalline powders [48, 49]. The microstructural and opto-electronic, charge transport, and magnetic properties were correlated with the preparation conditions (composition of precursor solution, post-deposition treatments, and cooling rate after the annealing) and with PV performances, to identify and understand the critical points that are hindering the production of high-performing solar cells based on high-quality CMTS thin films.

2. Experimental methods

A solution of $Cu(CH_3COO)_2{\cdot}H_2O$ (Sigma-Aldrich, purity $\geqslant$ 99%) in 2.5 ml of anhydrous dimethyl sulfoxide (Sigma-Aldrich purity $\geqslant$ 99.9%) was heated to 50 °C. $SnCl_2{\cdot}2H_2O$ (Alfa Aesar, purity 98%) was then added, changing the solution's color from blue to a transparent green. The mixture was stirred for 1 h at 50 °C. After cooling to room temperature, $Mn(CH_3COO)_2{\cdot}4H_2O$ (Merck Millipore, purity $\geqslant$99%) and thiourea (Fisher Scientific, purity $\geqslant$99%) were added. The resulting solution was a pale-yellow, transparent mixture, as previously optimized for CZTS. This solution was stirred overnight at room temperature, following the procedure reported elsewhere [35]. A 10% w/w aqueous KCl solution was then added to achieve a final concentration of 0.04 M, and the mixture was stirred for 30 min before deposition. The addition of KCl is known to form a liquid reactive phase (K_2S_x) during annealing, which facilitates crystallite coalescence and promotes the formation of large grains in CZTS thin films [50]. The entire procedure was performed in air.

Standard 2.2 mm-thick soda-lime glass (SLG, approximately 70% SiO_2, 15% Na_2O, and 9% CaO, with small amounts of other compounds) substrates were cleaned with a 15 min ultrasonic bath in a sequential series of solvents: acetone, Mucasol in distilled water, distilled water (4 times), acetone, and finally ethanol. The substrates were then dried under dynamic vacuum for 1 h. A 1.1 μm-thick Mo layer was deposited onto the SLG by DC magnetron sputtering, and the coated glass was cut into 3 cm^2 pieces. Before deposition, the Mo surface was subjected to a 45 min UV-O_3 treatment (Novascan PSD Pro Series—Digital UV Ozone System). The precursor solution was deposited using a blade-coating technique with a film applicator (Zehntner ZAA 2300, speed = 5 mm s^{-1}). The sample was left at room temperature for 30 min to undergo a sol-gel transition. The samples were then annealed in an argon-filled tubular oven with a heating rate of 17.5 °C min^{-1} from room temperature to 550 °C, followed by a 15 min isotherm at 550 °C in an inert atmosphere (5 N argon gas flux). The samples were then quenched to room temperature. This procedure was repeated four times to achieve the desired thickness. The thickness of all CMTS thin films was measured by profilometry, yielding an average of 2.5 $\pm$ 0.3 μm.

After annealing, the samples were quenched unless slow cooling (SC) was specified. Some selected samples were etched using an HCl solution. For characterization, freshly prepared samples were primarily used, while selected samples, stored for up to 9 months, were also used to evaluate potential aging effects. CdS layer was deposited via chemical bath deposition in an aqueous solution of NH_3 (Fisher Scientific 35% aqueous solution) and NH_4Cl (VWR Chemicals, purity 99.9%), using $Cd(CH_3COO)_2$ (Acros Organics, purity 98%) and thiourea at 75 °C. The CdS layer, as determined by profilometry, was 70–80 nm thick. The devices were completed with RF-sputtered i-ZnO and DC-pulsed sputtered Al:ZnO (AZO) as the top contact. The thicknesses of the i-ZnO and AZO layers were verified by profilometry, yielding 70 nm and 350 nm, respectively, as expected. An aluminum grid was then thermally evaporated to extract charges. Each device (active area of 0.16 cm^2) was electrically insulated by scribing the back contact. Some selected samples were subjected to TT at 260 °C [35].

CdS, i-ZnO, AZO, and aluminum layers were removed before the characterization presented here by immersing the sample in a 3 M HCl solution for 10 s and then in demineralized water. The procedure was repeated twice to ensure complete removal of the upper layers, and the samples were dried under a nitrogen flow.

X-ray diffraction (XRD) characterization was performed on a PANalytical X'Pert Pro MPD diffractometer equipped with an x-ray tube operating at 40 kV and 40 mA, providing Cu-Kα radiation

($\lambda = 1.540\ 56$ Å). For grazing incidence XRD (GI-XRD), a single-point detector with a parallel plate collimator was used. Grazing angles (ω) were set to 0.25°, 1.00°, 5.00°, and 10.00° to probe different depths of the thin film. A $(\frac{1}{16})°$ divergence slit and an 8 mm beam mask were selected. The scan range was $2\theta = 15°$ to $2\theta = 80°$, with a step size of 0.04°. The time per step was set at 10 s ($\omega = 1.00°$ and $\omega = 5.00°$) or 15 s ($\omega = 0.25°$ and $\omega = 10.00°$). A line detector was used for Bragg–Brentano XRD (BB-XRD). The BB-XRD diffractograms were acquired in $\theta/2\theta$ measurement mode. The scan range was $2\theta = 15°$ to $2\theta = 80°$, with measurement steps of 0.013°. The time per step was set at 0.195 s. A divergence slit of $(\frac{1}{4})°$ and a 7 mm beam mask were selected. Inorganic Crystal Structure Database (ICSD), licensed by FIZ of Karlsruhe, was used for phase recognition and peak attribution. The acquired diffractograms were then refined using the Le Bail method [51], which allows refinement even without *a priori* knowledge of the crystal structure, starting only from the space group. The refinement was performed using the Full Prof Suite software [52]. Peak shape was modeled using Thompson-Cox-Hastings pseudo-Voigt functions [53] to combine the Gaussian and Lorentzian contributions to peak broadening for the determination of microstructural parameters.

The thickness of each layer was measured by employing a Dektak 8 Stylus profiler. A 5 μm radius investigating tip was selected; the force applied to the surface samples was equivalent to 5 mg mass.

Kelvin probe (KP) and photoelectron yield spectroscopy (PYS) were combined to measure the work function (Φ) and ionization energy (E_i) of the prepared thin films, respectively, by employing a KP Technology SKP5050-APS02 setup under an ambient pressure environment of nitrogen gas, with the same experimental setup reported elsewhere [54]. The samples were contacted with carbon tape and mounted on a motorized 3-axis stage with a precision of less than 300 nm. The top counter electrode was a 2.0 mm diameter electrode with a gold-alloy coating.

KP measurements were carried out using a vibrating reference electrode, previously calibrated against a gold standard to determine its work function (Φ_{tip}). The sample work function (Φ_{sample}) was calculated using the equation: $\Phi_{sample} = \Phi_{tip} + e{\cdot}CPD$, where e is the elementary charge and CPD represents the contact potential difference measured between tip and sample. The CPD values were obtained with a precision of 1–3 mV. Surface photovoltage (SPV) was evaluated as the difference between the contact potential in light and dark conditions ($SPV = CPD_{light} - CPD_{dark} = \Phi_{light} - \Phi_{dark}$). A 670 nm laser diode (photon energy of 1.85 eV) with a power density of approximately 100 mW cm^{-2} was used for illumination. PYS was performed using the same KP setup operated in static mode, maintaining a tip-sample separation below 1 mm. A 10 V bias was applied to facilitate charge collection. The sample was exposed to UV light from a deuterium source coupled to a monochromator, allowing excitation in the 3.4–7.6 eV range. Spectra were recorded with 1 nm step increments, and the onset of photoemission was determined with an energy resolution of 30 meV. Total density of states spectra were obtained as the first derivative of the photoelectron yield with respect to photon energy. Further details on the KP-PYS setup and data evaluation can be found elsewhere [55].

A 660 nm diode laser was used as the source for photoluminescence (PL) measurements. A ¼ m InGaAs diode array was used as a detector. PL measurements were performed at room temperature.

J–V curves have been obtained through an ABET Technologies Sun 2000 Solar Simulator, equipped with a Keithley electrometer. The Xe-lamp calibration at 1.5 AM and 1000 W m^{-2} was performed at 25 °C using a silicon photodiode as the reference.

Magnetometric studies were performed on CMTS films directly grown on soda-lime glass substrate by means of a superconducting quantum interference device magnetometer (Quantum Design MPMS-XL5). The instrument allows direct control of both temperature (5–380 K) and magnetic field intensity (0–5 T). The $M(H)$ loop was measured at 300 K, with the magnetic field ranging from 5 T to −5 T, to investigate the magnetic character of the CMTS film. To fit the SQuID probe, the sample was divided into pieces and installed in the sample holder. Field cooling (FC) modes are then collected, ranging from 380 K to 5 K with an external magnetic field of 5000 Oe, high enough to overcome the diamagnetic contribution coming from the massive part of the sample, i.e. the glass substrate. Notably, the mass response of a diamagnetic material is indeed linearly dependent on the applied field but with a very low and negative slope parameter, whilst its magnetic moment is invariant vs temperature, i.e., magnetic volume susceptibility of glass $\chi_V = -1.128{\cdot}10^{-5}$ (International System, dimensionless) [56]. Unlike a paramagnetic material like CMTS, which is typically characterized by a higher, positive magnetic susceptibility and exhibits a substantial increase in the magnetic resultant as T decreases.

A Rigaku Miniflex 600 x-ray diffractometer, equipped with an x-ray tube operating at 40 kV and 15 mA, providing $\lambda = 1.5446$ Å, and a silicon array detector, was used to directly compare CMTS-1 grown on glass for magnetic measurements with CMTS-1 grown on molybdenum. The characterization was performed in BB geometry and in θ–2θ mode. The peaks were assigned based on data reported in the ICSD.

The transport characterization was performed by measuring the temperature-dependent resistivity using the Van der Pauw configuration. Four ohmic contacts were prepared by sputtering 100 nm-thick gold dots measuring 2 mm in size on the CMTS film, spaced approximately 10 mm apart in a square geometry. The four-wire probe resistivity measurement was performed using an Agilent 34 420 A, applying a 100 μA current between two contacts while simultaneously measuring the voltage across the opposite pair of contacts. The entire measurement was carried out under vacuum within a cryostat, cooling the film down to 70 K and then gradually heating up to 280 K, collecting one data point per K. For each temperature point, two independent measurements were performed according to the Van der Pauw method, using the two configurations obtained by rotating the current and voltage contacts by 90°. In this contact geometry, the two measured resistances (vertical resistance R_A and horizontal resistance R_B) were equal within the experimental error, allowing the use of the simplified expression $R_S \approx \frac{\pi}{\ln(2)} \cdot \frac{R_A+R_B}{2}$, where R_S is the sheet resistance of the sample, valid when $R_A \approx R_B$.

3. Results and discussion

The samples studied in this work were prepared over a long period; some were freshly prepared, while others (covered with CdS) were stored for up to 9 months. GIXRD ($\omega = 1.00°$) of both freshly prepared and stored for several months was performed (figure S1): no significant changes in XRD pattern were observed, suggesting no noticeable structural changes were induced during storage time.

3.1. Precursor composition

Structural characterization first aimed to determine the optimal metal ratio in the starting solution to obtain a pure, crystalline CMTS. A copper-poor composition was always kept since V_{Cu} has been reported to increase carrier density in various chalcogenide materials, with a beneficial effect on PV performances [29, 57]. The impact of the relative quantity of manganese and tin was investigated. The ratio of the components of the studied solution was varied, with [Mn]/[Sn] ranging from 1.00 to 1.13 and 1.27, as reported in table 1.

SOL-1, SOL-2, and SOL-3 were employed to prepare CMTS-1, CMTS-2, and CMTS-3, respectively. The elemental composition of CMTS-1, CMTS-2, and CMTS-3 was analyzed in a previous work [35] Using energy dispersive x-ray spectroscopy and x-ray photoelectron spectroscopy on thin films prepared with the same procedure, we found that the bulk composition perfectly follows the metals' ratio in the starting solution. Figure 1 reports x-ray diffractograms collected with different grazing angles and, hence, different penetration depths of CMTS-1, CMTS-2, and CMTS-3.

In all the x-ray diffractograms, peaks of the cubic molybdenum used as the substrate (space group $Im\bar{3}m$) are present [58]; their intensity increases with the increase of grazing angle, as expected. CMTS is present in the stannite-type structure (space group $I\bar{4}2m$) [48] with narrow peaks indicating a good crystalline quality. The peaks at $2\theta = 40.4°$ and $2\theta = 58.5°$ derive from the overlap between molybdenum and CMTS; they are attributed to the molybdenum since their intensity increases with the increase of grazing angle, so the contribution of the molybdenum to this signal is larger than the contribution of the stannite-type phase. No hints of secondary phases are detected using this technique. A closer look at GI-XRD (figure 2) reveals the presence of a 'step-like' shape on the left of the main peak between 26° and 27° in CMTS-2 and CMTS-3: this feature is typical of stacking faults [59, 60]. The presence of stacking faults appears to be directly related to the increase in the relative manganese content, as the typical shape is more pronounced in CMTS-3 than in CMTS-2. At the same time, it is completely absent in CMTS-1 at all the penetration depths. This feature is more pronounced at lower grazing angles, suggesting that stacking faults may be more concentrated in the outermost layers of CMTS. This phenomenon could be related to the presence of Cu_2SnS_3 (CTS) and MnS traces detected in CMTS-2 and CMTS-3 [35]. The presence of these secondary phases was confirmed by GIXRD analysis, and their previous detection by Raman spectroscopy was reported in ref. 35. It is important to emphasize that the samples used here are not the same as those in ref. 35, but were prepared using the same method described there. CTS, in particular, belongs to the same space group as CMTS ($I\bar{4}2m$) and, having the same crystal structure but lacking Mn, could give rise to stacking faults. CTS is more concentrated near the surface, since manganese is partially leached from the surface by ammonia during CdS deposition [35], thereby generating more stacking faults at lower incidence angles.

Le Bail refinement was used to determine the unit cell parameters, the coherent scattering domain size, and the average non-uniform microstrain, which induces peak broadening. Later on, 'microstrain' will always refer to non-uniform microstrain. The Le-Bail fittings are shown in **Note 1** in the supporting information. The unit cell parameters are reported in table 2, together with the estimated probing depth. The probing depth estimation method is reported in **Note 2** in the supporting information. Notably, a

Table 1. Ratio between components in the solutions utilized in this work. Note that the compositional ratios are integral values over the whole thin film.

Solution	$Cu(CH_3COO)_2$ $\bullet H_2O$ (M)	$SnCl_2\bullet 2H_2O$ (M)	$Mn(CH_3COO)_2$ $\bullet 4H_2O$ (M)	Thiourea (M)	[Mn]/[Sn]	[Cu]/([Mn]+[Sn])
SOL-1	0.356	0.200	0.200	3.6	1.00	0.89
SOL-2	0.356	0.188	0.212	3.6	1.13	0.89
SOL-3	0.356	0.176	0.224	3.6	1.27	0.89

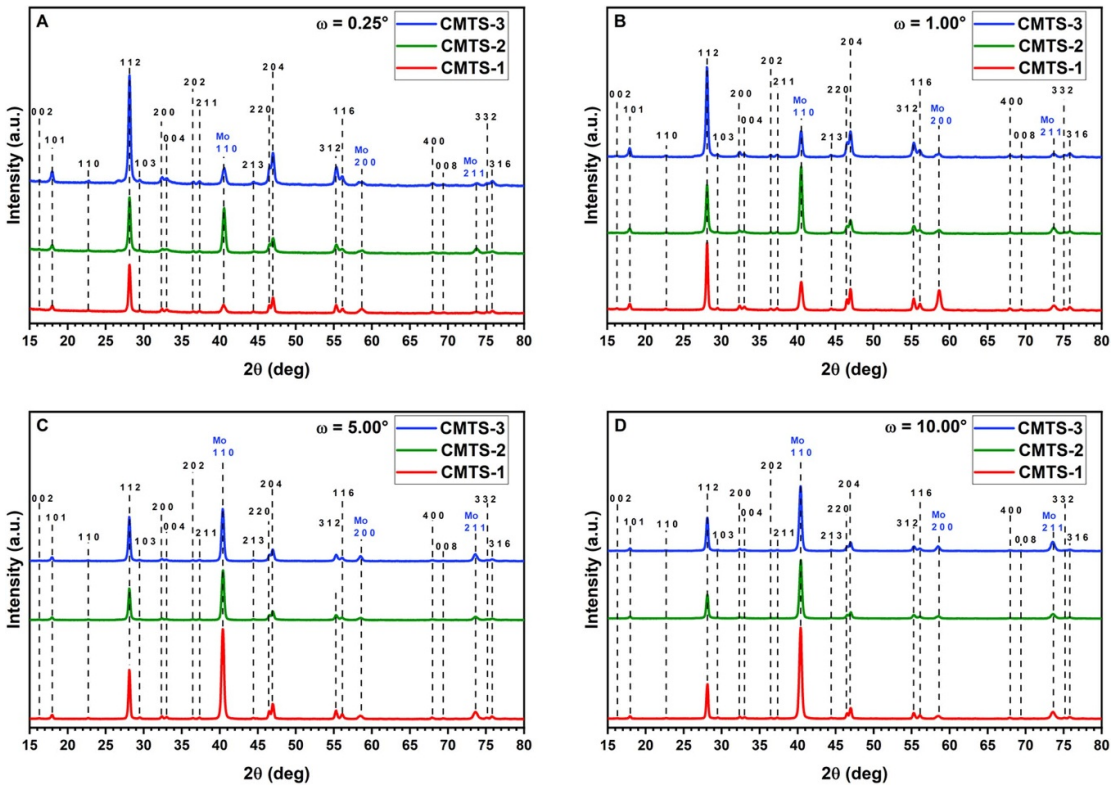

Figure 1. Grazing incidence diffractograms with peaks indexation for CMTS-1, CMTS-2 and CMTS-3 with $\omega = 0.25°$ (A), $\omega = 1.00°$ (B), $\omega = 5.00°$ (C), $\omega = 10.00°$ (D). The solid-dotted lines and black indexation indicate the Bragg peaks of CMTS according to the stannite-type structure.

slight reduction in the ***a*** and ***b*** parameters is observed from CMTS-1 to CMTS-3. This reduction could also be related to the presence of CTS, which shares the same space group as CMTS but exhibits a smaller unit cell in ***a*** and ***b*** directions [61]. A slight increase in the ***c*** parameter, leading to a higher tetragonal deformation parameter, is also reported. The tetragonal deformation parameter ($c/2a$) is less than 1 for all compositions, with a slight increase in distortion as the penetration depth increases. The $c/2a$ value is also slightly larger than that reported for CMTS in the stannite structure, which is typically <0.98 [46–48]. The deviation is more pronounced if the composition is off-stoichiometric (CMTS-2 and CMTS-3). The value increases from CMTS-1 to CMTS-3, indicating a greater deviation from the literature value for stannite-type CMTS with a larger manganese amount.

The average value of coherent scattering domain size (figure 3(A)) and microstrain (figure 3(B)) for CMTS-1, CMTS-2, and CMTS-3 has been extracted. Growing materials with large domain sizes is crucial for PV materials, since larger grains imply fewer grain boundaries, which have been reported to act as recombination sites in various PV materials [62, 63]. As shown in figure 3(A), CMTS-1 displays a much larger average domain size ($\geqslant$120 nm), even though precise estimation is hindered because the domain-size contribution to peak broadening falls below the instrument's resolution limit. In contrast, CMTS-2 and CMTS-3 consist of smaller domains, ranging from 41 to 64 nm for CMTS-2 and 44–91 nm for CMTS-3. It is worth noting that in CMTS-2 and CMTS-3, the average domain size increases with the grazing angle, indicating that crystallites are larger as we move into the bulk. It can be hypothesized that, because the CMTS thin film is composed of superimposed layers, excess sulfur vapor facilitates the recrystallization of the underlying layers during annealing, thereby favoring crystallite coalescence. The microstrain analysis confirms the higher quality of the CMTS-1 (figure 3(B)): its microstrain is much

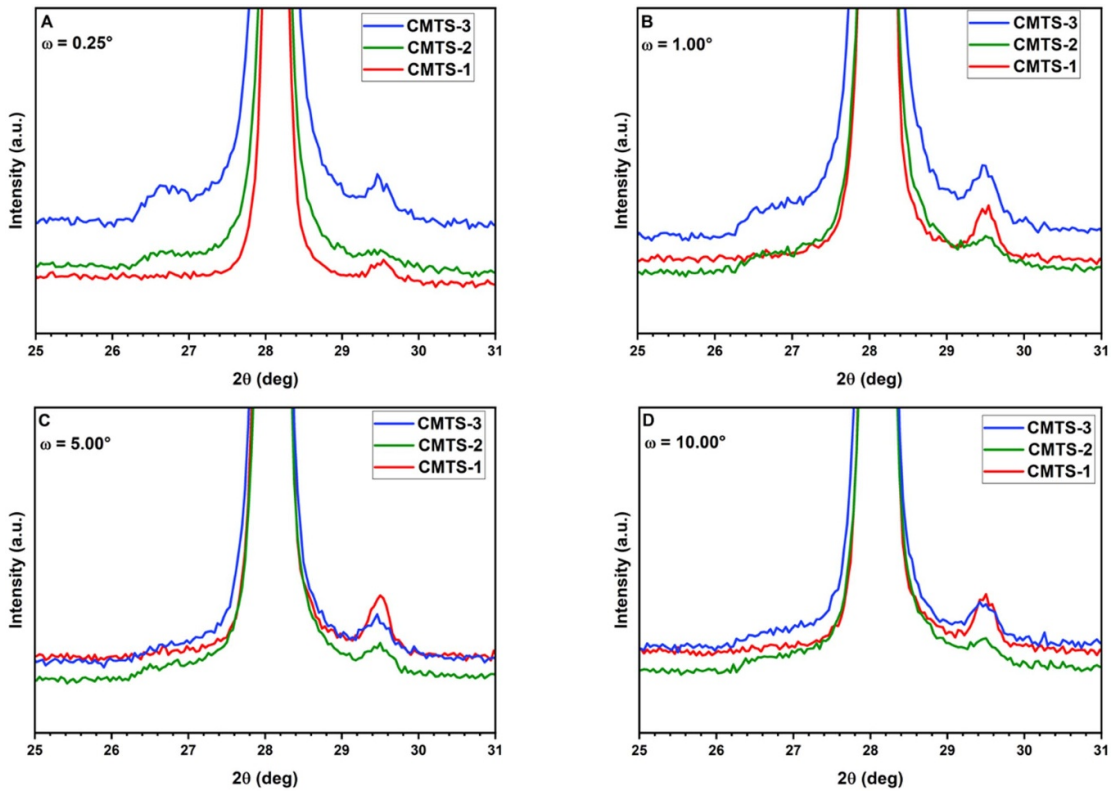

Figure 2. Grazing incidence diffractograms details of CMTS-1, CMTS-2 and CMTS-3 with $\omega = 0.25°$ (A), $\omega = 1.00°$ (B), $\omega = 5.00°$ (C), and $\omega = 10.00°$ (D).

Table 2. Variation of the unit cell parameters with the grazing incidence angle ω in CMTS-1, CMTS-2, and CMTS-3.

	ω (deg)	Probing depth (μm)	$a = b$ (Å)	c (Å)	$c/2a$
CMTS-1	0.25	0.07 ± 0.01	5.515 ± 0.001	10.824 ± 0.003	0.9813 ± 0.004
	1.00	0.28 ± 0.01	5.514 ± 0.001	10.824 ± 0.002	0.9815 ± 0.004
	5.00	1.40 ± 0.01	5.513 ± 0.001	10.824 ± 0.002	0.9817 ± 0.004
	10.00	2.79 ± 0.01	5.514 ± 0.001	10.824 ± 0.002	0.9817 ± 0.004
CMTS-2	0.25	0.07 ± 0.01	5.511 ± 0.001	10.827 ± 0.003	0.9823 ± 0.004
	1.00	0.28 ± 0.01	5.510 ± 0.001	10.825 ± 0.003	0.9823 ± 0.004
	5.00	1.40 ± 0.01	5.510 ± 0.001	10.824 ± 0.003	0.9822 ± 0.004
	10.00	2.79 ± 0.01	5.511 ± 0.001	10.827 ± 0.003	0.9823 ± 0.004
CMTS-3	0.25	0.07 ± 0.01	5.510 ± 0.001	10.828 ± 0.003	0.9826 ± 0.004
	1.00	0.28 ± 0.01	5.509 ± 0.001	10.827 ± 0.003	0.9827 ± 0.004
	5.00	1.40 ± 0.01	5.508 ± 0.001	10.826 ± 0.003	0.9828 ± 0.004
	10.00	2.79 ± 0.01	5.508 ± 0.001	10.826 ± 0.003	0.9828 ± 0.004

lower than that of the other two samples. Also, CMTS-3 is more strained than CMTS-2, indicating that adding excess manganese introduces stress in the film. In all the compositions, the lower microstrain has been detected in the diffractogram collected with $\omega = 1.00°$: the average microstrain is higher close to the top surface ($\omega = 0.25°$) and close to the interface with the back contact (more contribution at high grazing incident angle, $\omega = 5.00°$, $\omega = 10.00°$) than in the bulk.

The x-ray diffractogram of CMTS in the BB configuration was collected to determine if there was any family of planes with a preferential orientation parallel to the thin film surface; a single crystal pattern [42] was used to derive the crystal structure information file and, consequently, to calculate the expected powder pattern for a perfectly random-oriented sample. The normalized BB-XRD of randomly oriented reference and BB-XRD of CMTS-1 (figure 4(A)), CMTS-2 (figure 4(B)), and CMTS-3 (figure 4(C)) are reported in figure 4. The intensity of the 1 1 2 reflection was found to be over-represented, meaning that the corresponding lattice plane is preferentially oriented parallel to the sample plane. In fact, the $I_{1\,1\,2}/I_{\text{tot}}$ ratio (the ratio between the intensity of 1 1 2 peak and the sum

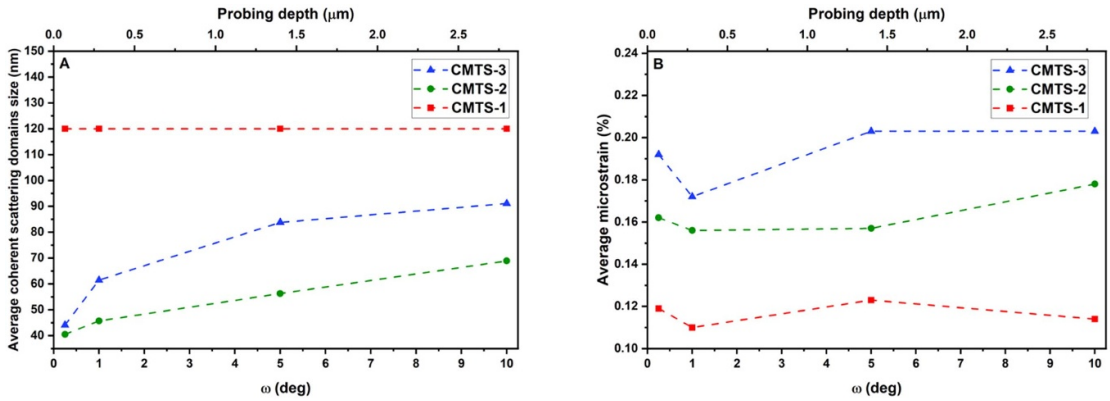

Figure 3. Extracted average value of coherent scattering domain size (A) and microstrain (B) for CMTS-1, CMTS-2, and CMTS-3.

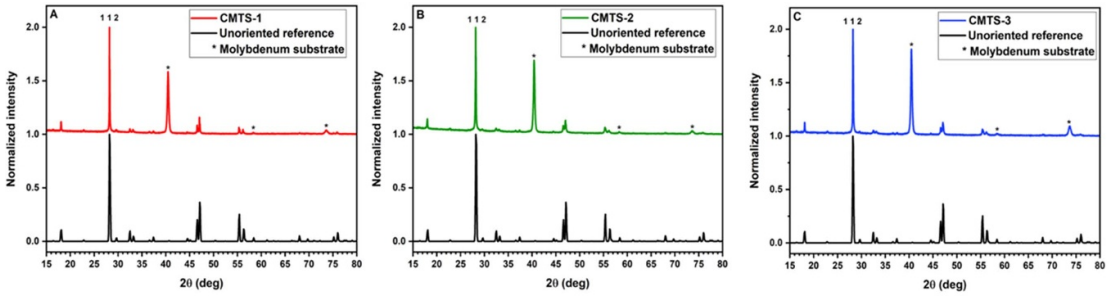

Figure 4. Comparison between an unoriented CMTS reference and BB-XRD of: CMTS-1 (A), CMTS-2 (B), CMTS-3 (C). The Bragg peaks of the molybdenum substrate are marked with *.

of the intensity of all the peaks) is equal to 0.38 in the calculated randomly oriented pattern; all the examined samples showed higher values, with 0.46 (CMTS-1), 0.57 (CMTS-2), and 0.49 (CMTS-3).

PL spectra of CMTS-1, CMTS-2, and CMTS-3, collected at room temperature, are shown in figure 5(A). The spectrum of CMTS-1 is also shown in figure 5(B), with a different scale for clarity. They all display the main PL peak at 1.4 eV, at energies lower than E_g (1.5–1.6 eV) [35], which can be related to the band-tailing phenomenon [64]; a PL peak at 1.4 eV has been experimentally found in CZTS and attributed to band-to-tail transition [65], in which the recombination is between a hole in the tail of the valence band and a free electron. Moreover, the theoretical work from Chen and Persson [66] predicts a reduction between 0.1 and 0.2 eV of the CMTS band gap, as was found in this study, linked to the presence of copper–manganese antisites. A shoulder at 1.35 eV is observed in CMTS-1 and CMTS-3, whereas in CMTS-2 it is not visible due to broadening of the main peak; this peak has already been observed in CZTS and is attributed to the deep antisite defect Cu_{Sn} [67]. The increase in the manganese/tin ratio from CMTS-1 to CMTS-3 (table 1) strongly increases the intensity of the emission peak, indicating a longer carrier lifetime.

Photoelectron yield spectroscopy and KP measurements have been employed to depict band positions. They are reported in figure 6. The cubic root extrapolation of the photoelectron yield, as a function of incident photon energy, allows the calculation of the ionization energy, and hence valence band maximum (VBM) of the material, through the x-axis intercept (figure 6(A)) [55, 68]. The ionization energy, E_i, varies from 4.97 eV for CMTS-1 5.15 eV for CMTS-2, and it was found to be 5.03 eV for CMTS-3; therefore, the ionization energy increases with increasing relative manganese content. Work function (measured by KP) and hence Fermi level value for CMTS-1, CMTS-2, and CMTS-3 are 4.98 eV, 5.00 eV, and 5.01 eV, respectively (figure 6(C)). It can be noticed that CMTS-1 is a degenerate film (E_F–$E_{VBM} > 0$) and hence with high hole concentration. The addition of manganese suggests a quenching of the degeneracy (E_F–$E_{VBM} < 0$), slightly shifting the VBM energy (E_{VBM}) downwards, with a more pronounced effect on CMTS-2. The work function remains constant under both dark and light conditions. Hence, no SPV is detected in any of the three compositions, following the outcomes of the absent PV performance recorded for devices as fabricated [35].

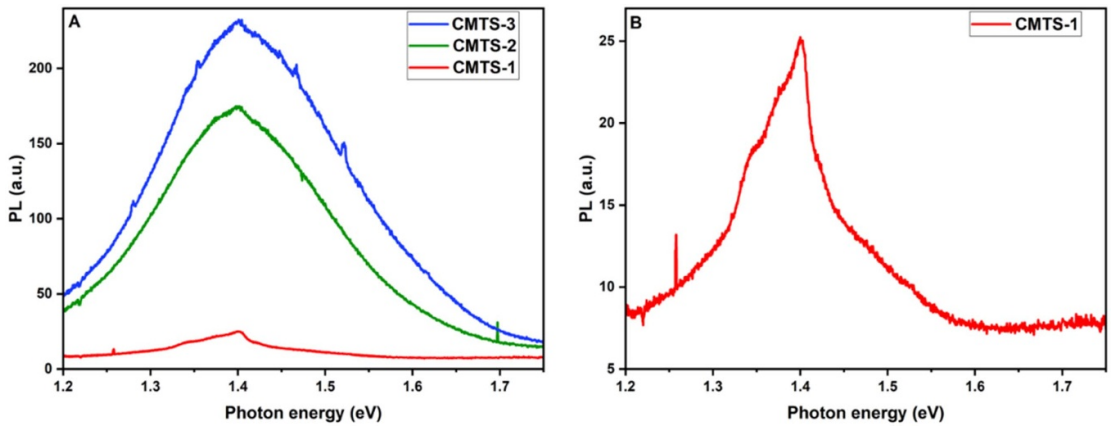

Figure 5. (A) PL spectra of CMTS-1 (red), CMTS-2 (green), and CMTS-3 (blue) collected at room temperature: (B) magnification of the PL spectrum of CMTS-1.

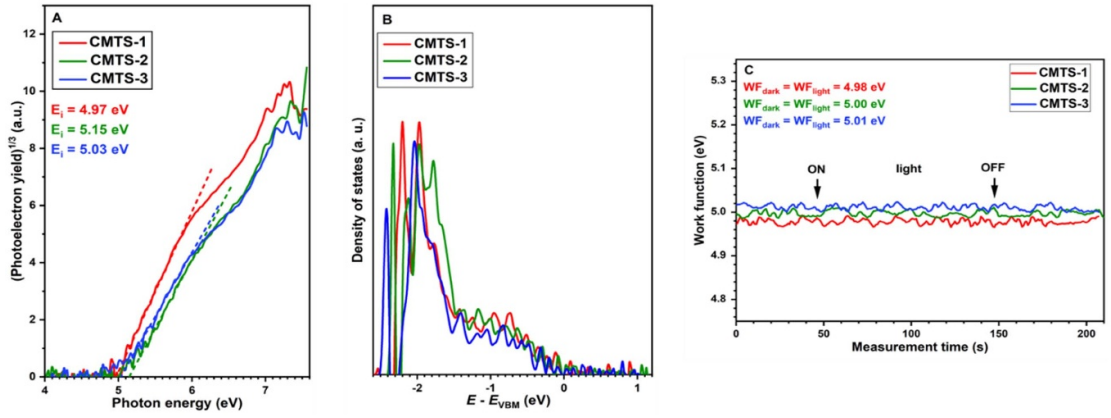

Figure 6. Photoelectron yield spectra with determined ionization energies (A), valence band total density of states spectra (B), and work function in dark and light conditions (C) of CMTS-1 (red), CMTS-2 (green), and CMTS-3 (blue).

To sum up, the findings of GI-XRD measurements confirmed that SOL-1 is the most adequate composition [35], since it exhibits larger domain sizes (figure 3(A)), less microstrain (figure 3(B)), and no stacking faults were detected (figure 2). Its crystallographic parameters are more coherent with typical stannite-type CMTS values.

3.2. Post-deposition treatments

The first post-deposition treatment studied was the etching of the absorber with a 3% HCl solution, at 75° for 10 min, before the buffer layer deposition. An inset of GI-XRD at different penetration depths ($\omega = 0.25°$, 1.00°, 5.00° and 10°) is reported in figure S2 (CMTS-2) and figure S3 (CMTS-3). It is possible to note a reduction in the features typical of stacking faults; the effect is more pronounced at low grazing angles, where stacking faults are more concentrated. The unit cell parameters of the etched samples are reported in table 3. The etching process does not impact **a** parameter. CMTS-1 and CMTS-2 show a strong contraction along the crystallographic *c*-axis due to the etching treatment, which lowers the tetragonal deformation parameter *c*/2*a*. In CMTS-3, elongation along the crystallographic *c*-axis is detected at low grazing angles ($\omega = 0.25°$, 1.00°) and is limited to the uppermost layers. A contraction at higher grazing angles ($\omega = 5.00°$, $\omega = 10.00°$), probing the bulk, was observed, as already reported for CMTS-1 and CMTS-2. The tetragonal deformation parameter is lower than 1 for all the compositions examined. The etching process can remove traces of secondary phases [33], thereby leading to *c*/2*a* values closer to literature ones for CMTS [46–48], as a consequence of the contraction along the *c*-axis.

The average size of the coherent scattering domains in CMTS-1, with and without etching, is reported in figure 7(A). After the etching treatment, the average size is still ⩾120 nm. The average microstrain at different grazing angles for etched (orange line) and not-etched (red line) thin films is reported in figure 7(B). HCl etching shows a beneficial effect on the microstrain of CMTS-1, reducing the stress

Table 3. Variation of the unit cell parameters with the grazing incidence angle in CMTS-1, CMTS-2, and CMTS-3 after HCl etching.

	ω (deg)	Probing depth (μm)	$a = b$ (Å)	c (Å)	$c/2a$
MTS-1_etched	0.25	0.07 ± 0.01	5.516 ± 0.001	10.806 ± 0.002	0.9795 ± 0.004
	1.00	0.28 ± 0.01	5.516 ± 0.001	10.809 ± 0.002	0.9798 ± 0.004
	5.00	1.40 ± 0.01	5.517 ± 0.001	10.816 ± 0.003	0.9802 ± 0.004
	10.00	2.80 ± 0.01	5.518 ± 0.001	10.818 ± 0.003	0.9803 ± 0.004
CMTS-2_etched	0.25	0.07 ± 0.01	5.512 ± 0.001	10.818 ± 0.003	0.9813 ± 0.004
	1.00	0.28 ± 0.01	5.511 ± 0.001	10.816 ± 0.003	0.9813 ± 0.004
	5.00	1.40 ± 0.01	5.511 ± 0.001	10.822 ± 0.003	0.9819 ± 0.004
	10.00	2.79 ± 0.01	5.512 ± 0.001	10.821 ± 0.003	0.9816 ± 0.004
CMTS-3_etched	0.25	0.07 ± 0.01	5.510 ± 0.001	10.834 ± 0.003	0.9831 ± 0.004
	1.00	0.28 ± 0.01	5.509 ± 0.001	10.830 ± 0.003	0.9829 ± 0.004
	5.00	1.40 ± 0.01	5.510 ± 0.001	10.827 ± 0.003	0.9825 ± 0.004
	10.00	2.79 ± 0.01	5.509 ± 0.001	10.826 ± 0.003	0.9826 ± 0.004

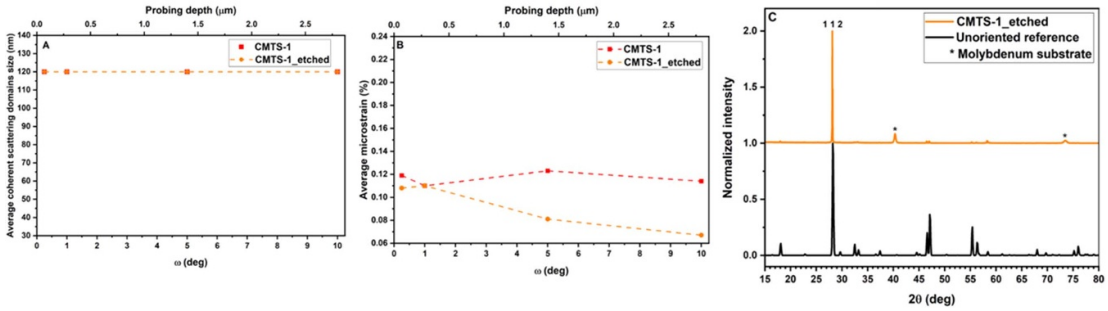

Figure 7. Effect of etching on average coherent scattering domain size (A), average microstrain (B), and preferred orientations (C).

observed at all the different grazing angles. The impact of HCl etching on the microstructural parameters of CMTS-2 and CMTS-3 is shown in figures S4 and S5. Moreover, even the size of coherent scattering domains is positively affected by HCl etching. In CMTS-2_etched, the size spans from 41 to $\geqslant$120 nm, while in etched CMTS-3, it spans from 50 to 100 nm; in addition, in both etched and non-etched samples, the increase in the domains' average size at higher grazing angles is observed. The average microstrain in CMTS-3 is reduced by HCl etching, as in CMTS-1, whereas the opposite is observed in CMTS-2.

Normalized BB-XRD of CMTS-1 etched is reported in figure 7(C), together with a completely unoriented powder pattern, calculated from the crystal structure information derived from [42]. It is noticeable that after the HCl etching, the (112) lattice plane preferred orientation is much more pronounced than before ($I_{1\,1\,2}/I_{\mathrm{tot}} = 0.84$). Normalized BB-XRD of CMTS-2 and CMTS-3 are reported in figure S6. The preferred orientation of the (1 1 2) plane in CMTS-2_etched ($I_{1\,1\,2}/I_{\mathrm{tot}} = 0.74$) is intensified as in CMTS-1_etched, while CMTS-3_etched shows almost unchanged intensities after the HCl etching ($I_{1\,1\,2}/I_{\mathrm{tot}} = 0.50$).

The increase in the average coherent scattering domain size after the etching treatment suggests that HCl may also wash out smaller CMTS grains, thereby raising the average domain size. Besides, smaller CMTS grains likely tend to be less oriented, while large columnar domains could be more subject to a specific growth direction; the intensification of (1 1 2) preferred orientation after HCl etching could be another hint towards the removal of smaller CMTS grains by HCl, consequently increasing the portion of CMTS exhibiting a preferred growth direction.

The effect of the etching on the PL spectrum of CMTS-1 is depicted in figure S7. The main peak is still centered at 1.4 eV; the same considerations reported above can be applied. The broad signal at 1.35 eV, attributed to the deep defect Cu_{Sn}, splits into two lower-intensity peaks, suggesting a reduction in its formation. HCl etching does not affect the electronic structure of CMTS; in fact, there is a negligible difference in ionization energy (figure S8(A)) and work function (figure S8(C)). Again, the work function value does not change upon illumination (i.e. SPV was still not detected) as expected, since no working device was obtained without TT [35]. Degeneracy is still detected, as E_F–$E_{VBM} > 0$, which hampers device efficiency.

Table 4. Variation of the unit cell parameters with the grazing incidence angle in CMTS-1 after the thermal treatment.

	ω (deg)	Probing depth (μm)	$a = b$ (Å)	c (Å)	$c/2a$
CMTS-1_TT	0.25	0.07 ± 0.01	5.514 ± 0.001	10.839 ± 0.002	0.9829 ± 0.004
	1.00	0.28 ± 0.01	5.512 ± 0.001	10.837 ± 0.002	0.9830 ± 0.004
	5.00	1.40 ± 0.01	5.511 ± 0.001	10.840 ± 0.002	0.9835 ± 0.004
	10.00	2.80 ± 0.01	5.511 ± 0.001	10.842 ± 0.002	0.9837 ± 0.004

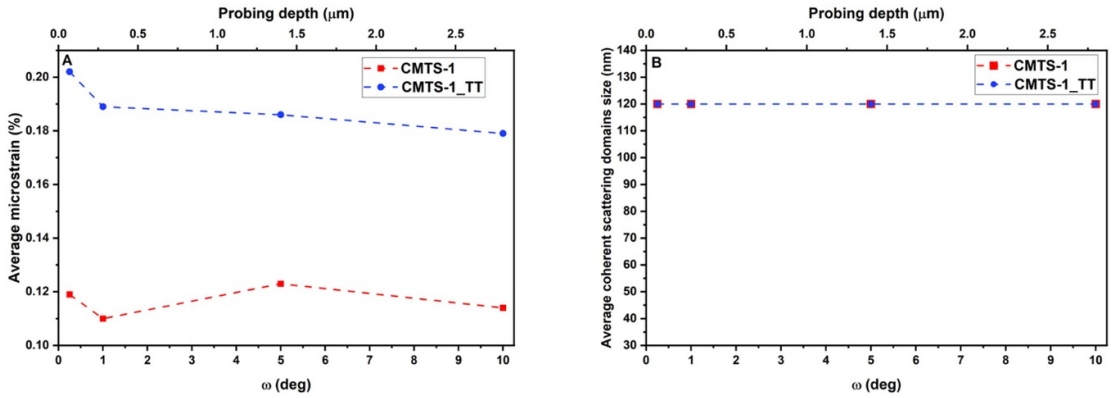

Figure 8. Extracted average value of microstrain (A) and coherent scattering domain size (B) for CMTS-1 with (blue) and without (red) thermal treatment.

Consequently, the TT effect of the complete device (at 260 °C for 10 min) has been evaluated. Structural parameters have been extracted through Le-Bail refinement and are reported in table 4. A considerable elongation along the c-axis is observed, resulting in a substantial increase in the tetragonal deformation parameter $c/2a$ at all penetration depths. In contrast, it increases with increasing grazing angle, as previously described for untreated thin films. TT also causes a strong increase of 50% in the average microstrain (figure 8(A)). The microstrain reaches its maximum close to the surface, with a grazing angle of $\omega = 0.25°$. These results suggest TT favors Cd diffusion from CdS to the absorber, as already proposed [69, 70]. Cd^{2+} can substitute for the isovalent Mn^{2+}, which is partially lost during CdS deposition [35], in the stannite structure, leading to both a microstrain increase and an elongation of the cell, given the much bigger ionic radius of Cd^{2+} than Mn^{2+} [15]. Moreover, Cd diffusion is also consistent with the reported [35] strong increase in V_{OC} after TT, suggesting a beneficial effect of Cd diffusion on the CMTS/CdS junction. The loss maps of CMTS-based solar cells indicated that TT primarily improves the p–n junction, thereby reducing CdS defectivity at the CMTS interface [33]. The average size of coherent scattering domains (figure 8(B)) is not influenced by TT, with values $\geqslant$120 nm in both cases.

The TT does not impact the (1 1 2) preferred orientation parallel to the sample plane, which is retained ($I_{(1\,1\,2)}/I_{tot} = 0.57$), and the normalized BB-XRD of CMTS-1_TT shows almost the same pattern as CMTS-1 (figure S9). PL spectrum of CMTS-1_TT (figure S10) exhibits the same shape as CMTS-1, but with a reduced intensity, suggesting that the TT induces shorter carrier lifetime and lower carrier concentration [71]. Photoelectron yield spectroscopy and work function measurements of CMTS-1 pre and post TT are reported in figure 9. Electronic characterization confirms the beneficial effect of TT. After TT, the ionization energy increases, from 4.97 eV to 5.12 eV (figure 9(A)). As a consequence, TT induces the beneficial effect of degeneracy elimination (i.e. E_F–$E_{VBM} < 0$). However, no SPV is detected (figure 9(C)), presumably due to Fermi level pinning caused by the high density of surface defects.

The combination of HCl etching and TT results in an 'intermediate' state in which the effects of both post-deposition treatments are visible (table 5). The ***c*** parameter is larger than CMTS-1 for the impact of cadmium diffusion favored by TT (as discussed above) but smaller than CMTS-1_TT, confirming the beneficial effect of HCl etching. The tetragonal deformation value ~~comprises~~ comprises the CMTS-1 value and the CMTS-1 value after TT.

The microstrain analysis confirms the intermediate situation (figure 10(B), black line). The microstrain coefficient of CMTS-1 after etching and TTs is consistently between 0.144% and 0.165%. This value lies between CMTS-1 and CMTS-1_TT, reflecting the combined effects of etching (reducing microstrain) and TT (increasing microstrain). The average size of coherent scattering domains (figure 10(A), black line) is 68 nm and 112 nm at $\omega = 0.25°$ and $\omega = 1.00°$, respectively, showing

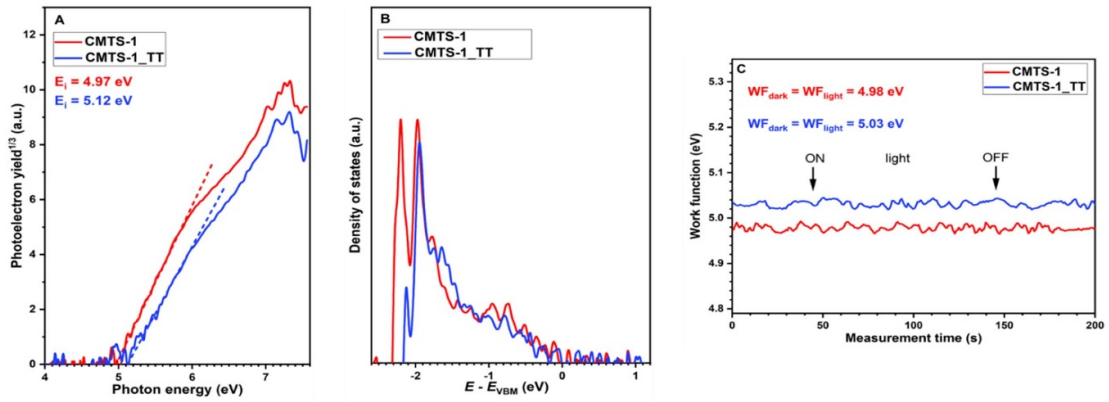

Figure 9. Photoelectron yield spectra with determined ionization energies (A), valence band total density of states spectra (B), and work function in dark and light conditions (C) of CMTS-1 with (blue) and without (red) thermal treatment.

Table 5. Parameters of the unit cell with the grazing incidence angle in CMTS-1 after HCl etching and thermal treatment.

	ω (deg)	Probing depth (μm)	$a = b$ (Å)	c (Å)	$c/2a$
CMTS-1_etched and TT	0.25	0.070	5.515 ± 0.001	10.830 ± 0.003	0.9819 ± 0.004
	1.00	0.281	5.513 ± 0.001	10.829 ± 0.002	0.9821 ± 0.004
	5.00	1.402	5.512 ± 0.001	10.826 ± 0.002	0.9820 ± 0.004
	10.00	2.795	5.513 ± 0.001	10.827 ± 0.003	0.9820 ± 0.004

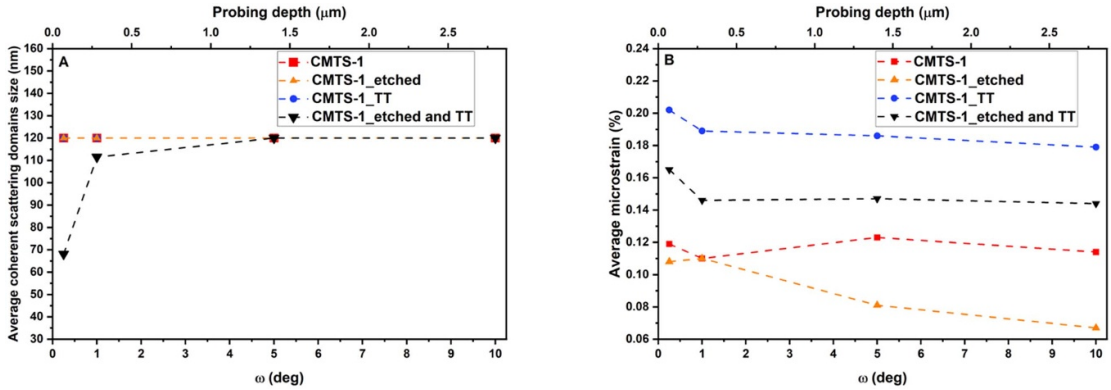

Figure 10. Extracted average value of coherent scattering domains size (A) and microstrain (B) for CMTS-1 with and without etching and thermal treatment.

a reduction, compared to CMTS-1, close to the surface; however, probing the bulk at larger grazing angles, ($\omega = 5.00°$ and $\omega = 10.00°$) the size of the domains is >120 nm (the peaks broadening due to the particle size is too close to the instrumental resolution), as it was for the other samples of CMTS-1. The combined effect of HCl etching and TT yields the best-performing devices [35]: in particular, TT increased mainly V_{OC}, as already discussed, while etching enhances the crystallinity of the CMTS, thereby increasing all PV parameters.

The preferred orientation estimate is reported in figure S11. It can be seen that this combined treatment also does not affect the (1 1 2) preferred orientation parallel to the sample plane, which is retained ($I_{112}/I_{tot} = 0.47$), with a pattern very similar to that of untreated CMTS-1. The electronic characterization (figure 11) also confirms the beneficial effect of etching and TT. The combined treatments induce a further increase in ionization energy than TT alone, reaching 5.24 eV (figure 11(A)). The degeneracy is thereby quenched (E_F–VBM < 0), and the Fermi-level pinning is reduced, as it is needed to obtain a working device. Moreover, as shown in figure 11(C), the work function under illumination (5.14 eV) differs from that in the dark (5.11 eV), indicating a SPV.

In the PL spectrum (figure 12), the main peak at 1.4 eV, derived from a band-to-tail transition, as discussed above in the text, is retained. Two peaks at about 1.2 eV appeared, related to a deeper

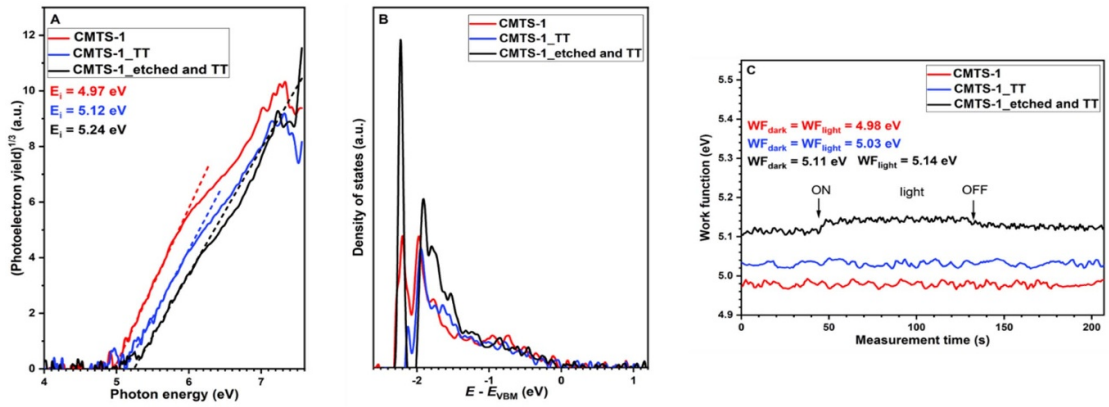

Figure 11. Combined effect of etching and thermal treatment on ionization energy (A), valence band total density of states (B), and work function in the dark and under illumination (C).

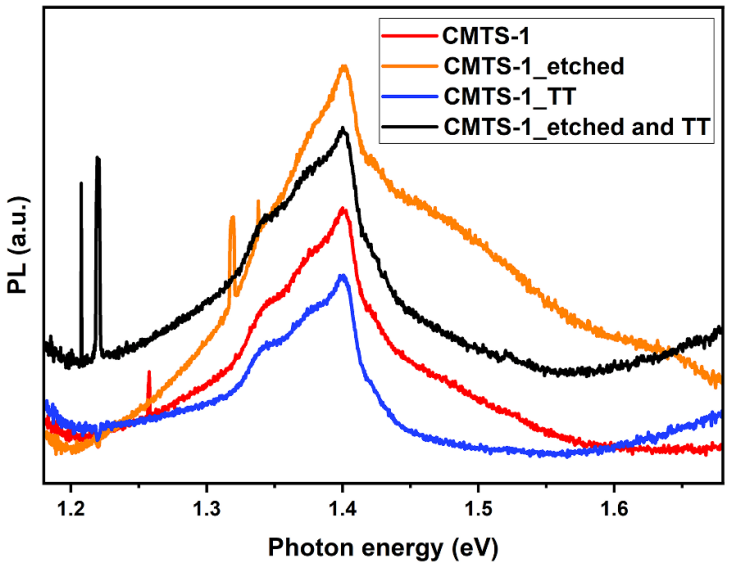

Figure 12. Combined effect of etching and TT on PL spectrum.

Table 6. Summary of the effect of composition and post-deposition treatments on microstructure, optoelectronics, and PV performances.

	CMTS-1	CMTS-2	CMTS-3	CMTS-1 etched	CMTS-1 TT	CMTS-1 etched and TT
Average domain size (nm)	⩾120	41–69	44–91	⩾120	⩾120	⩾120
Average microstrain (%)	0.110–0.123	0.156–0.178	0.172–0.203	0.067–0.110	0.186–0.202	0.144–0.165
Ionization energy (eV)	4.97	5.15	5.03	5.01	5.12	5.24
Degeneracy (y/n)	y	n	n	y	n	n
V_{OC} (mV)	93.1	14.8	—	—	192.3	245.5
J_{SC} (mA cm^{-2})	2.46	2.92	—	—	3.9	4.9
FF (%)	29.4	12.1	—	—	31.5	39.6
η (%)	0.07	0.01	—	—	0.24	0.48

defect within the CMTS band gap. The beneficial reduction in intensity from TT is confirmed (black line versus orange line). Table 6 summarizes the influence of starting solution composition and post-deposition treatments on the microstructural parameters, optoelectronic properties, and PV performance of the corresponding champion device.

Table 7. Parameters of the unit cell with the grazing incidence angle in CMTS-1 subjected to slow cooling, before (CMTS-1_SC) and after the thermal treatment (CMTS-1_SC and TT).

	ω (deg)	Probing depth (μm)	$a = b$ (Å)	c (Å)	$c/2a$
CMTS-1_SC	0.25	0.070	5.517 ± 0.001	10.819 ± 0.003	0.9805 ± 0.004
	1.00	0.281	5.515 ± 0.001	10.816 ± 0.002	0.9806 ± 0.004
	5.00	1.403	5.515 ± 0.001	10.818 ± 0.002	0.9809 ± 0.004
	10.00	2.797	5.516 ± 0.001	10.819 ± 0.002	0.9809 ± 0.004
CMTS-1_SC and TT	0.25	0.070	5.514 ± 0.001	10.837 ± 0.002	0.9827 ± 0.004
	1.00	0.281	5.512 ± 0.001	10.837 ± 0.002	0.9830 ± 0.004
	5.00	1.403	5.511 ± 0.001	10.839 ± 0.002	0.9834 ± 0.004
	10.00	2.796	5.511 ± 0.001	10.839 ± 0.002	0.9834 ± 0.004

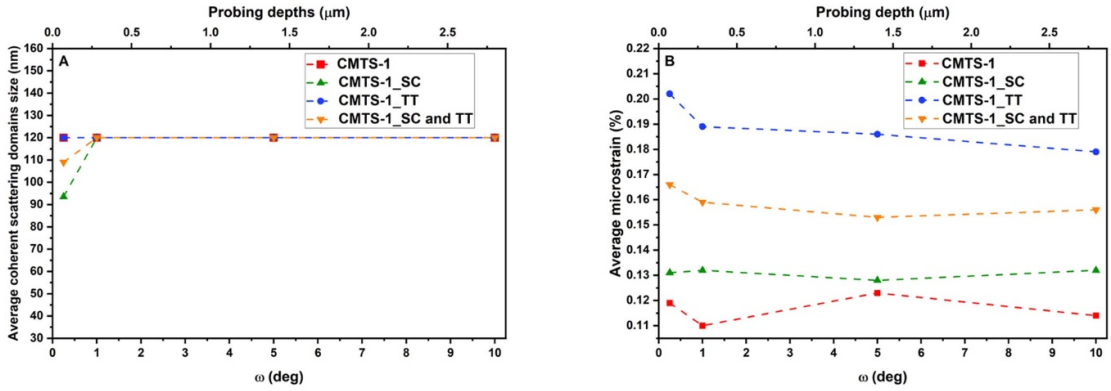

Figure 13. Effect of slow cooling before (green) and after (orange) the thermal treatment on the average size of coherent scattering domains (A) and average microstrain (B).

3.3. SC

A strategy of SC rather than quenching after the annealing step was applied to CMTS-1 to reduce defectivity and avoid mechanical stress arising from the different thermal coefficients between CMTS and the molybdenum film on the glass substrate. Etching was not performed on CMTS-1_SC to study the effect of cooling rate, separately for pre- and post-TT. CMTS-1_SC has been reported to have an E_g of 1.6 eV; upon TT, E_g shifts to 1.5 eV, the same as that measured for CMTS-1 [35]. The unit cell parameters of slow-cooled samples, pre and post TT, are reported in table 7. The CMTS-1_SC exhibits a slight reduction in the c parameter compared to CMTS-1 and, hence, a lower value of the tetragonal deformation parameter, approaching those of highly crystalline CMTS [46–48]. CMTS-1_SC and TT, instead, show the same parameters as CMTS-1_TT, indicating that Cd diffusion is still occurring (the $c/2a$ parameter remains increased) regardless of the cooling rate used to prepare the sample.

As shown in figure 13(A), both SC samples exhibit coherent scattering domains larger than 120 nm, with the CMTS-1 having a slightly lower value, particularly near the surface (i.e. $\omega = 0.25°$). The average microstrain of CMTS-1_SC, represented by the green line in figure 13(B), is almost the same as that of CMTS-1, with a negligible value difference. In CMTS-1_SC and TT (orange line), microstrain shifts upward, indicating cadmium interdiffusion, as discussed above, although it does not reach the values observed in CMTS-1_TT, maintaining a more ordered and compact structure than CMTS-1_TT. The BB-XRD of CMTS-1_SC pre- and post-TT is shown in figure S12. The cooling rate does not influence the preferred orientations. (1 1 2) preferred orientation parallel to the sample plane is retained, with a very similar pattern to quenched samples ($I_{1\,1\,2}/I_{tot} = 0.50$ for CMTS-1_SC and $I_{1\,1\,2}/I_{tot} = 0.52$ for CMTS-1_SC and TT).

The electronic characterization of the SC samples is reported in figure 14. CMTS-1_SC shows a higher ionization energy (5.19 eV) compared to 4.97 eV of CMTS-1 (figure 14(A)). At the same time, E_i is reduced to 5.10 eV, in CMTS-1_SC and TT, with value similar to CMTS-1_TT (5.12 eV), indicating a substantial equivalence after TT, regardless of the cooling rate. The work function in the dark and under

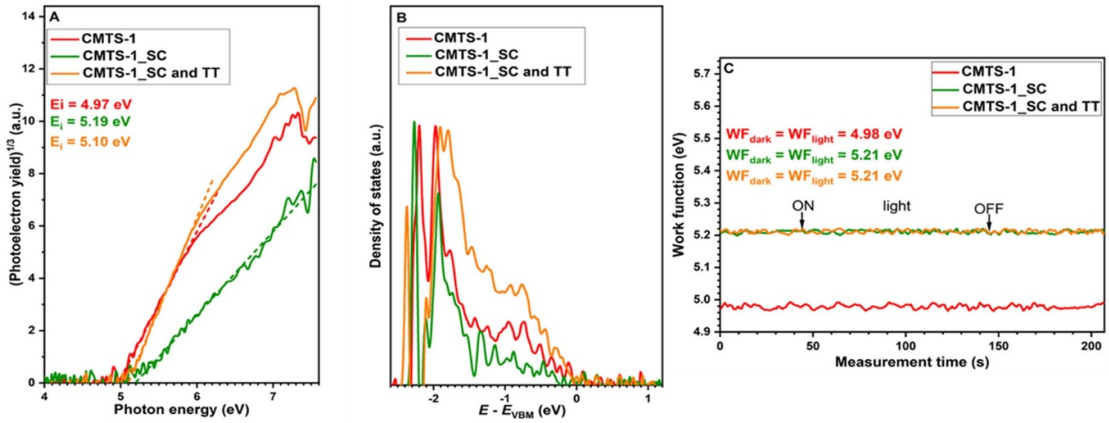

Figure 14. Comparison of the effect of slow cooling before (green) and after (orange) the thermal treatment with CMTS-1 without treatments (red) on ionization energy (A), valence band total density of states (B), and work function in the dark and under illumination (C).

light is 5.21 eV for both SC samples (figure 14(C)). Thus, no SPV has been detected, and the samples show degeneracy (E_F–VBM > 0).

The PL spectrum of the SC samples (figure S13) is similar to previous ones, with the main peak centered at 1.4 eV, corresponding to a band-to-tail transition. The reduction of the intensity upon TT has also been confirmed.

Working devices have been obtained from slow-cooled samples, as shown in figure 15, where the PV parameters required for the power conversion efficiency calculation are also reported. A solar cell's parameters are derived from its current–voltage density (J–V) curve under standard illuminated conditions. This curve yields critical values, such as the open-circuit voltage (V_{oc}), which is the maximum voltage at zero current, and the short-circuit current density (J_{sc}), which is the maximum current density at zero voltage. Another key parameter is the fill factor (FF), which quantifies the solar cell's ideality [72]. The study of the optical bandgap of thin CMTS reported in our previous work [35] showed that E_g is approximately 1.5 eV. SC samples are the only ones in which PV conversion has been demonstrated without TT, achieving 0.40% efficiency as deposited. The attainment of a working device without the TT could be linked to the high ionization energy of the CMTS-1_SC sample, as reported in figure 14 (a higher ionization energy was found to be beneficial also in the case of CMTS-1_TT and CMTS-1_etched and TT) and also to a reduction in mechanical stress between CMTS and the molybdenum film on the substrate during the contraction due to the cooling after the annealing process. After TT, efficiency increased to 0.58% due to cadmium diffusion, as discussed above. The champion device was stored at room temperature in the dark to study the effect of aging, which has been reported to improve the efficiency of the CMTS-based devices [33, 35]. The sample CMTS-1_SC and TT reached a new record efficiency for wet-prepared CMTS, with $\eta = 0.97\%$, 5 months after the first J–V measurement. Performance improvement upon aging can be ascribed to interdiffusion at the CZTSSe/CdS interface, such as reduced lattice mismatch and an increase in the conduction band offset, as demonstrated for the CZTSSe/CdS interface [73]. Still, the PV performances are far from theoretical expectations: considering that it is a quaternary chalcogenide with a bandgap of 1.5 eV, its ideal theoretical efficiency would be approximately 28.7% [74]. This value represents the ideal maximum efficiency of a direct-bandgap semiconductor under standard illumination conditions, ignoring all non-fundamental losses. For example, the junction between the absorbing semiconductor and the buffer layer is crucial. The commonly used buffer layer, CdS, induces losses in CMTS-based devices related to the non-optimal band alignment with the absorber [35] and issues related to transparency: CdS shows more than 90% transmittance for photons with $\lambda \geqslant 600$ nm but absorbs blue and near-UV light (figure S14), thus reducing photon availability for PV conversion. Moreover, all chalcogenide-based solar cells suffer from potential loss at the back interface with the Mo contact, as the sulfurization or selenization step in the production process results in the formation of a $Mo(S, Se)_2$ layer [33, 75]. The interface with the back contact creates a resistive barrier that hinders charge carrier transport, increasing the cell's series resistance and, consequently, significantly reducing the FF and overall efficiency. However, in the case of CMTS, PV

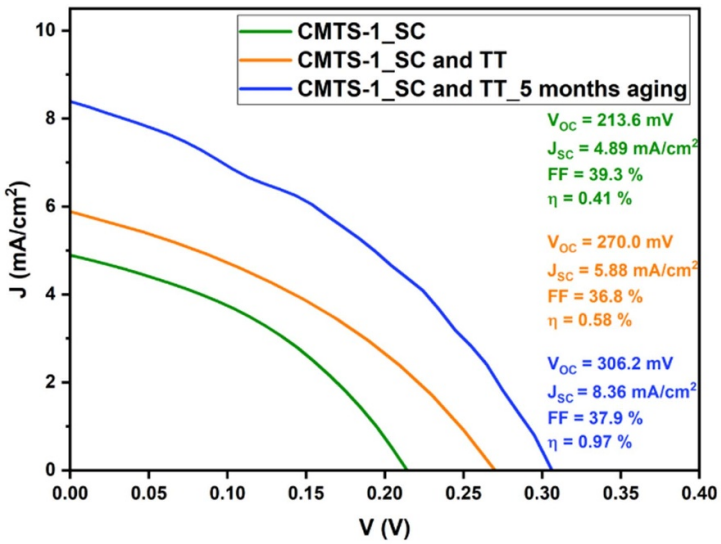

Figure 15. *J–V* curves of the champion device of CMTS-1 slow-cooled pre (green) and post (orange) thermal treatment.

performance remains too poor to be attributed to issues common to other chalcogenide-based thin-film technologies. Digging into the current literature, it is clear that research on this compound is still in its infancy, so the 'non-fundamental losses' are poorly understood; yet they are likely significant enough to hinder the development of functional PV devices.

3.4. Magnetic and transport characterization

The magnetic properties of the material do not directly influence light absorption, which is determined by its band structure. However, they can significantly impact the dynamics of photogenerated charge carriers. In a material with non-ideal magnetic behavior, spin recombination can serve as a channel for energy loss, thereby reducing the device's overall efficiency [44, 45]. To investigate this, the magnetic moment (expressed in electromagnetic units, emu) was measured at 300 K over the range −50 kOe to 50 kOe to determine the magnetic character of the CMTS-1 thin film. CMTS-1 was chosen as it shows the best properties among the compositions tested, and it was prepared on SLG for this characterization to avoid Mo magnetic contribution. CMTS could form with different structures on glass and on molybdenum, so the BB-XRD pattern of CMTS-1 grown on glass was directly compared with those of CMTS etched with TT and without post-deposition treatments, both grown on Mo (figure S15). CMTS-1 grown on glass exhibits the same characteristic reflections, thus confirming the adoption of the stannite crystal structure; moreover, no hints of secondary phases, due to the growth on glass, could be observed. A morphological comparison between CMTS films deposited on SLG and on Mo-coated SLG (figure S16) revealed that the former exhibit significantly larger (one order of magnitude) grains than those grown on Mo. The larger grain size observed in CMTS films grown on SLG is attributed to the well-known sodium diffusion from the substrate during annealing, which promotes recrystallization and grain coarsening, as reported for other chalcogenide absorbers such as CIGS and CZTS. Conversely, when Mo is used as a back contact, partial formation of MoS_2 acts as a diffusion barrier, reducing Na incorporation and limiting grain growth [18, 75–81].

Nevertheless, estimating the mass magnetization is challenging to elaborate on due to the lack of information in the literature on the material density and the difficulty of measuring the mass of such a thin film using standard weighing procedures. Even if the CMTS films were deposited on SLG substrates rather than Mo/SLG to isolate the intrinsic magnetic signal of CMTS, the total signal would still be affected by the diamagnetic contribution from the glassy substrate, which cannot be quantitatively estimated because its magnitude is close to the instrument's sensitivity limit. But, despite the different substrates, XRD confirmed an identical stannite crystal structure for both configurations. At the same time, SEM revealed larger grains on glass, a morphology promoted by Na diffusion from the substrate as discussed [18, 75–81]. This microstructural difference reduces edge-related artifacts and enhances the representativeness of the intrinsic magnetic response, so primarily reflecting the bulk-like properties of

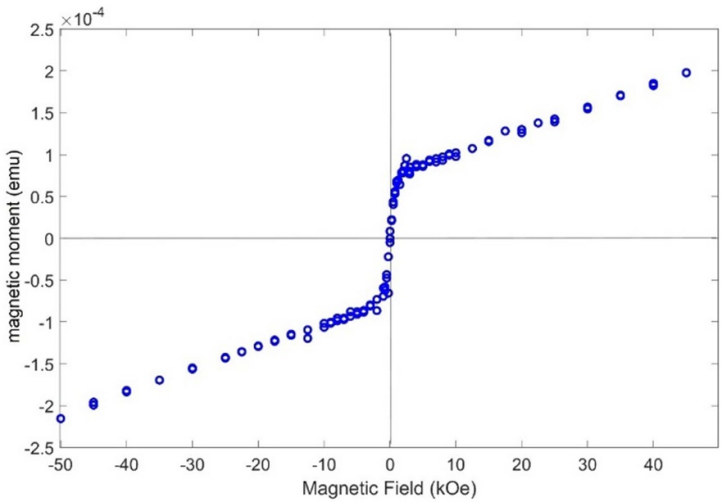

Figure 16. Hysteresis loop collected at 300 K between −50 kOe and 50 kOe for CMTS-1 film.

the CMTS phase. Besides, it should be emphasized that the absolute values reported in emu represent raw magnetic moments and they are not normalized to the sample volume or mass. This choice was intentional, as the diamagnetic contribution of the glass substrate and the weak film signal do not allow for a quantitative estimation of the overall magnetic moment. Consequently, the following discussion focuses exclusively on the temperature- and field-dependence of the magnetic response, providing reliable qualitative insight into the intrinsic behavior of CMTS. This approach is consistent with common practice in the magnetic characterization of thin films and nanostructured systems, where absolute calibration is often hindered by substrate contribution or by extremely small sample mass [82–84].

The results reported in figure 16 indicate a non-paramagnetic magnetic response at room temperature in the CMTS film. In particular, the $M(H)$ curve exhibits s-shaped hysteresis loop with negligible coercivity and remanence, consistent with very soft magnetic behavior associated with weak or disordered magnetic interactions [82–84]. The origin of magnetism in CMTS thin films, already reported in literature [38, 42, 43], could primarily be attributable to Mn^{2+} ions, whose electronic configuration ($3d^5$) gives five unpaired electrons, which can promote a static magnetic moment [41]. Indeed, the increasing linear trend of the magnetic resultant at higher (negative or positive) fields preliminarily suggests a more complex behavior of the system. Linear trends in the $M(H)$ loop in the intermediate or high regime can be a fingerprint of the superposition of at least two magnetic contributions, for instance, a weakly hysteretic component (coming from a ferro(-i)magnetic or weak ferromagnetic phase) and a linear contribution compatible with paramagnetic or antiferromagnetic responses. However, the presence, in traces, of ferromagnetic or antiferromagnetic impurity in concentrations below the sensitivity threshold of the applied structural and morphological experimental techniques (GI-XRD) can be ruled out since compounds containing Mn^{2+} and sulfur, which show ferro or ferri- or antiferromagnetism at RT, have never been reported so far in literature. This suggests that the extrinsic (spurious) presence of a magnetic contaminant can be excluded, thereby ruling out the coexistence of two distinct magnetic populations and their corresponding contributions. Notably, such a kind of field-dependence can also arise in a spin-canted non-collinear antiferromagnetic material [85, 86], which usually displays weak ferromagnetic resultant [87, 88], or even in strong correlated/disordered magnetic systems, like the case of spin glass materials [89, 90].

To gather more information on CMTS magnetism and to understand the behavior observed in the $M(H)$ loop, $M(T)$ FC measurements have been collected at 5000 Oe, starting from the maximum temperature allowed by the magnetometer (380 K). A particularly high field is required to enhance the magnetic response of the paramagnetic film, which has negligible mass with respect to the diamagnetic substrate. Also, it is important to note that, due to the weak magnetic response of the thin films, the measurements reported here cannot be strictly quantitatively interpreted. The contribution from the diamagnetic substrate introduces a constant background, preventing an accurate determination of the absolute magnetic moment. For this reason, the analysis focuses on the relative evolution of the magnetic moment with field and temperature, which remains a reliable indicator of the magnetic behavior of the CMTS phase, as previously discussed [82– 84]. Figure 17(A) indeed shows that the thermal trend of

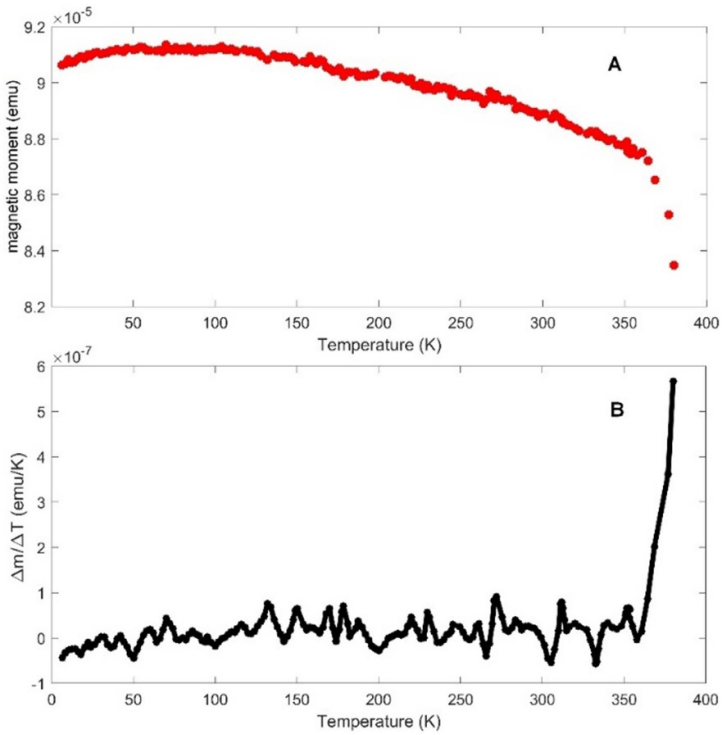

Figure 17. $M(T)$ FC recorded at 5000 Oe for CMTS-1 (A) and the discrete incremental ratio $\Delta M/\Delta T$ of the curve (B).

magnetization indicates no hyperbolic dependence of M on T, ruling out, once again, the possibility of a disordered paramagnetic state in CMTS. On the other hand, two notable features stand out:

(1) During the cooling ramp (from 380 to 360 K), a marked increase in magnetization is observed, suggesting the gradual formation of a magnetic ordering dynamics, most likely a crossover from a predominantly disordered paramagnetic regime to a regime characterized by interacting magnetic moments. However, the instrument's maximum operating temperature prevented tracking the transition to its completion and confirming the full return to the paramagnetic regime. Consistently, the derivative $\Delta M/\Delta T$ does not exhibit a well-defined peak, indicating that the transition is still in progress (figure 17(B)).
(2) Upon further cooling, the magnetization shows a continuous increase instead of stabilizing at a constant value, as would occur in a conventional ferromagnetic state. Below approximately 50 K, a small downturn in magnetization is observed, consistent with the freezing of frustrated magnetic states characteristic of spin-glass systems [91–93].

The behavior described in observation (2) clarifies the interpretation of figure 16. While the field-dependent $M(H)$ curve could initially suggest a mixed contribution from ferromagnetic and paramagnetic phases, the temperature-dependent response in figure 17 contradicts this view: the absence of a Curie-like upturn and the slight downturn below 50 K indicate that the magnetism does not arise from coexisting magnetic populations, but rather from a single, intrinsically disordered magnetic phase exhibiting short-range correlations. In fact, a hyperbolic Curie increase of the overall magnetic signal vs $1/T$ should be observed in the correspondence of a flat regime of the ferro(-i) phase response, whether a paramagnetic phase would be coexistent in the material; however, this is not observed. Therefore, the results of these magnetometric studies are compatible with an RT inhomogeneous magnetic system, possibly characterized by short-range interaction, as reported for other chalcogenides [94]. However, due to the CMTS film's small volume and related instrumental limitations, dedicated future studies (possibly on CMTS cm-sized single crystals) are needed to confirm or invalidate this claim.

The presence of a weakly ordered, spin-glass-like magnetic state may therefore be consistent with the semimetallic character previously proposed for CMTS [30, 38, 39]. Such intrinsic magnetic disorder may influence charge carrier localization and scattering, ultimately affecting the film's transport properties. To explore this correlation, Van der Pauw characterization was performed on a CMTS-1 thin film, grown on a glass substrate, to isolate its transport properties. The measurement was collected between 76 and

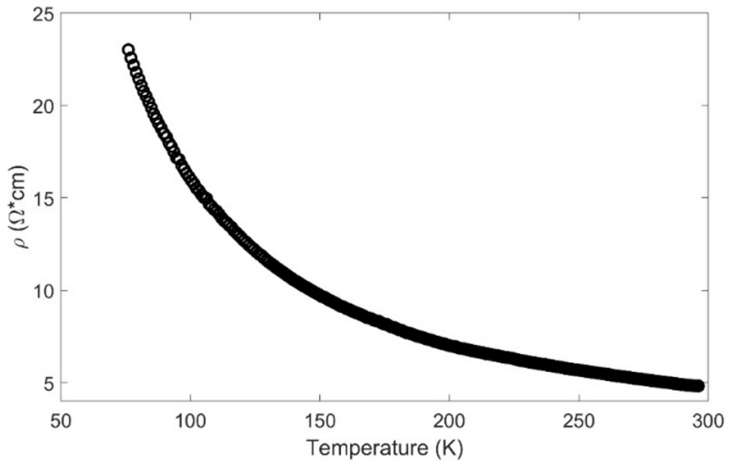

Figure 18. Sheet resistivity for the CMTS-1 film, collected through the Van der Pauw protocol between 76 K and 296 K.

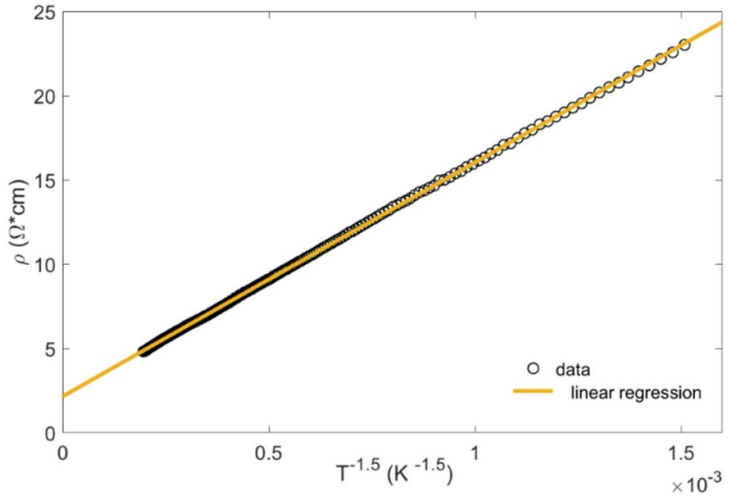

Figure 19. Linear regression of the resistivity curve of CMTS-1 resistivity vs temperature imposing a $T^{-3/2}$ dependence. The interpolating law $\rho = a \cdot T^{-\frac{3}{2}} + b$ returns as best fit parameters $a = 1.389{\cdot}10^4$ Ω·cm·K$^{3/2}$ and $b = 2.153$ Ω·cm.

296 K and is shown in figure 18. The RT sheet resistivity was 4.83 Ω·cm, consistently with the previous reported resistivity value [39]. It increased by less than an order of magnitude (to 23.02 Ω·cm) at the lowest tested temperature. At first glance, the resistivity trend could qualitatively appear to decrease with temperature, following the thermally activated exponential law $\rho = \rho_0 \cdot e^{-E/K_B \cdot T}$ as predicted for standard semiconductors [95]. However, a detailed analysis (reported in figure S17) revealed that the Arrhenius plot systematically deviates from linearity at higher temperatures, with negative residuals, suggesting that the resistivity reduction (i.e., the occupation of the conductive band) is non-exponential or it is hindered by carrier scattering.

Conversely, the overall decrease of resistivity with increasing temperature rules out a metallic conduction mechanism in CMTS. Then, a simple power law was applied instead of the classical exponential thermal-activated semiconductor law to describe the transport mechanism. Best fitting results were obtained by plotting ρ vs $T^{-3/2}$, resulting in an $R^2 = 0.9999$ (figure 19). This kind of thermal behavior of the transport properties has already been observed in semimetals [96–100], suggesting that CMTS material may have a low electronic energy gap despite an optical band gap typical of a semiconductor. This behavior is consistent with the literature [30, 38, 39], and, indeed, the semimetallic nature of CMTS has been identified as a factor contributing to its limited PV performance. Hall measurements from similar films have revealed a carrier density on the order of 10^{19}–10^{20} cm^{-3} [30, 38], which is too high for an ideal solar absorber. This high density leads to a very narrow depletion region, resulting in a low J_{SC}. Furthermore, the enhanced Auger recombination process, a consequence of the high carrier concentration, significantly shortens the minority carrier lifetime and, consequently, reduces the V_{OC} [30].

Taken together, the field- and temperature-dependent measurements provide additional insight into the magnetic nature of CMTS. While the $M(H)$ curve alone could be interpreted as the superposition of a ferromagnetic-like and a linear paramagnetic contribution, the temperature-dependent magnetization clarifies this behavior. Under a high applied field of 5000 Oe, the magnetic moment increases only gradually as the temperature decreases from 350 K to about 50 K, suggesting a progressive development of magnetic interactions. Below 50 K, however, the signal slightly decreases rather than continuing to rise, which excludes a paramagnetic component that would instead follow a Curie-type divergence. The coexistence of an S-shaped $M(H)$ loop with negligible coercivity and residual magnetization, and a non-Curie $M(T)$ trend, suggests a magnetically disordered state with short-range correlations, consistent with spin-glass-like behavior. Here, the term 'spin-glass-like' is used strictly as a phenomenological descriptor of the observed $M(T)$ and $M(H)$ trends, without implying a definitive classification of the magnetic ground state. This interpretation is supported by structural and compositional analyses that exclude secondary paramagnetic phases and is consistent with previous reports on magnetic frustration/inhomogeneity in related chalcogenide systems [38, 42, 43, 94]. It should be noted that this conclusion remains a working hypothesis, as low-field AC susceptibility or ZFC/FC measurements, required to fully confirm spin-glass ordering, are currently unfeasible for thin films, due to their low mass and the resulting weak signal-to-noise ratio. CMTS single crystals should be synthesized specifically. Overall, the magnetic results support the view that CMTS exhibits weakly ordered, possibly frustrated spin interactions. Although the weak signal intensity prevents quantitative analysis, the qualitative consistency of the $M(H)$ and $M(T)$ trends supports the presence of intrinsic magnetic ordering phenomena, even at RT in CMTS. Overall, along with its semimetallic transport, these findings provide a comprehensive explanation for the device's low PV efficiency, demonstrating that the material's intrinsic semimetallic nature, together with short range inhomogeneous magnetic order already settled at ambient conditions, contributes to its limited PV performance. At the same time, this understanding opens new perspectives for exploiting CMTS in alternative, spin-dependent, or magnetically active energy applications.

4. Conclusions

This work has determined the crystallographic and electronic structure of CMTS thin films prepared from solution methods. It has also studied the influence of several preparation parameters on the quality of the final material and correlated these parameters with the previously reported PV performance. The influence of the starting solution composition was studied, revealing the optimal metal ratio to obtain a more crystalline film with lower microstrain and larger crystallites. The importance of CMTS surface etching with HCl solution was demonstrated, enhancing crystalline quality and further reducing microstrain. Thermal treatment at 260 °C of the complete devices was found to be crucial for favoring Cd diffusion at the CMTS/CdS interface, thereby improving the p–n junction and refining the band alignment, increasing the ionization energy of CMTS and thus removing the degeneracy. The combined effect of these two post-deposition treatments yields a high-quality CMTS film with the best-reported PV parameters; thermal treatment at the junction enhances V_{OC}, while etching of the material itself improves all PV parameters. The slow cooling of the device's material after annealing results in a more compact structure with reduced mechanical stress at the back-contact interface. Preliminary studies on devices made with slow-cooled CMTS and a new record for wet-processed CMTS thin films ($\eta = 0.97\%$) have been achieved. Since the efficiency remains below 1%, the reasons behind the typical low efficiencies of CMTS-based PV devices have been investigated. Intra-gap defects detected by PL analysis can act as recombination centers, thereby severely affecting the PV performance. Moreover, the results discussed indicate room-temperature coexistence of semimetallic-like behavior and a short-range magnetic-ordered state, as inferred from qualitative magnetometric characterization, which is not optimal for a PV absorber. This interplay between magnetism and carrier transport, though detrimental for PV efficiency, unveils a distinctive physical landscape that could be harnessed in other spin-dependent or thermomagnetic energy applications. In future studies, preparation and characterization of CMTS cm-sized single crystals will be required to investigate these properties comprehensively.

Data availability statement

Data supporting the findings of this study are available within the article and its supplementary materials.

Additional data available at http://doi.org/10.1088/2515-7655/ae42f1/data1.

Acknowledgment

The article is based upon work from COST Action Research and International Networking project 'Emerging Inorganic Chalcogenides for PVs (RENEW-PV),' CA21148, supported by COST (European Cooperation in Science and Technology).

This study is a result of the research project 'nuovi Concetti, mAteriali e tecnologie per l'iNtegrazione del fotoVoltAico negli edifici in uno scenariodi generazione diffuSa' [CANVAS], funded by the Italian Ministry of the Environment and Energy Security, through the Research Fund for the Italian Electrical System (type-A call, published on G.U.R.I. n. 192 on 18-08-2022).

The author F.B. acknowledges the Dottorato di Interesse Nazionale 'Photovoltaics'.

The authors gratefully acknowledge Dr Hannes Hempel for technical support.

Conflict of interest

The authors declare no competing financial interest.

Author contributions

Fabio Butrichi 0000-0003-1762-8163
Conceptualization (equal), Data curation (equal), Formal analysis (equal), Investigation (equal), Methodology (equal), Software (equal), Visualization (equal), Writing – original draft (equal), Writing – review & editing (equal)

Giorgio Tseberlidis 0000-0002-9224-180X
Conceptualization (equal), Investigation (equal), Supervision (equal), Validation (equal), Writing – review & editing (equal)

Vanira Trifiletti 0000-0003-4066-3426
Conceptualization (equal), Formal analysis (equal), Investigation (equal), Methodology (equal), Supervision (equal), Validation (equal), Writing – original draft (equal), Writing – review & editing (equal)

Davide Delmonte 0000-0001-5367-527X
Data curation (equal), Investigation (equal), Methodology (equal), Software (equal), Validation (equal), Writing – original draft (equal)

Matteo Bronzoni 0000-0002-8513-8978
Data curation (equal), Investigation (equal), Validation (equal), Visualization (equal)

René Schwiddessen
Data curation (equal), Formal analysis (equal), Investigation (equal), Methodology (equal), Software (equal), Visualization (equal), Writing – original draft (equal)

Galina Gurieva 0000-0001-8609-1043
Data curation (equal), Formal analysis (equal), Investigation (equal), Methodology (equal), Supervision (equal), Validation (equal), Writing – original draft (equal), Writing – review & editing (equal)

Marin Rusu 0000-0002-1429-0219
Data curation (equal), Formal analysis (equal), Investigation (equal), Methodology (equal), Supervision (equal), Validation (equal), Writing – review & editing (equal)

Simona Binetti 0000-0002-8605-3896
Funding acquisition (equal), Project administration (equal), Resources (equal), Supervision (equal), Validation (equal)

Susan Schorr 0000-0002-6687-614X
Conceptualization (equal), Formal analysis (equal), Funding acquisition (equal), Methodology (equal), Project administration (equal), Resources (equal), Supervision (equal), Writing – review & editing (equal)

References

[1] Machín A and Márquez F 2024 Advancements in photovoltaic cell materials: silicon, organic, and perovskite solar cells *Materials* **17** 1165
[2] Li X, Li P, Wu Z, Luo D, Yu H-Y and Lu Z-H 2021 Review and perspective of materials for flexible solar cells *Mater. Rep.: Energy* **1** 100001
[3] Tai Y, Zhang X, Li J, Zheng Y, Liu G, Zhang J, Zeng G, Yakubov K and Alla C 2025 Research on ultra-thin cadmium telluride heterojunction thin film solar cells *Renew. Sustain. Energy Rev.* **207** 114996
[4] Machkih K, Oubaki R and Makha M 2024 A review of CIGS thin film semiconductor deposition via sputtering and thermal evaporation for solar cell applications *Coatings* **14** 1088
[5] Saparov B 2022 Next generation thin-film solar absorbers based on chalcogenides *Chem. Rev.* **122** 10575–7
[6] Gu S, Ullah S, Khan F, Wang X, Liu P, Yang S and Chen Y 2024 Recent advances and perspectives on Sb_2S_3 thin-film solar cells *Mater. Today* **28** 101019
[7] Cantas A, Gundogan S H, Turkoglu F, Koseoglu H, Aygun G and Ozyuzer L 2023 Photovoltaic performance of magnetron sputtered antimony selenide thin film solar cells buffered by cadmium sulfide and cadmium sulfide/zinc sulfide *Thin Solid Films* **784** 140070
[8] Jakomin R, Rampino S, Spaggiari G and Pattini F 2023 Advances on Sb_2Se_3 solar cells fabricated by physical vapor deposition techniques *Solar* **3** 566–95
[9] Schorr S, Gurieva G, Guc M, Dimitrievska M, Pérez-Rodríguez A, Izquierdo-Roca V, Schnohr C S, Kim J, Jo W and Merino J M 2020 Point defects, compositional fluctuations, and secondary phases in non-stoichiometric kesterites *J. Phys.* **2** 012002
[10] Giraldo S, Jehl Z, Placidi M, Izquierdo-Roca V, Pérez-Rodríguez A and Saucedo E 2019 Progress and perspectives of thin film kesterite photovoltaic technology: a critical review *Adv. Mater.* **31** 1806692
[11] Isotta E, Syafiq U, Ataollahi N, Chiappini A, Malerba C, Luong S, Trifiletti V, Fenwick O, Pugno N M and Scardi P 2021 Thermoelectric properties of CZTS thin films: effect of Cu–Zn disorder *Phys. Chem. Chem. Phys.* **23** 13148–58
[12] Trifiletti V, Mostoni S, Butrichi F, Acciarri M, Binetti S and Scotti R 2019 Study of precursor-inks designed for high-quality Cu_2ZnSnS_4 films for low-cost PV application *Chemistry Select* **4** 4905–12
[13] Tseberlidis G, Gobbo C, Trifiletti V, Di Palma V and Binetti S 2024 Cd-free kesterite solar cells: state-of-the-art and perspectives *Sustain. Mater. Technol.* **41** e01003
[14] Green M A, Dunlop E D, Yoshita M, Kopidakis N, Bothe K, Siefer G, Hao X and Jiang J Y 2025 Solar cell efficiency tables (version 66 *Prog. Photovolt.* **33** 795–810
[15] Shannon R D 1976 Revised effective ionic radii and systematic studies of interatomic distances in halides and chalcogenides *Acta Crystallogr. A* **32** 751–67
[16] Romanyuk Y E, Haass S G, Giraldo S, Placidi M, Tiwari D, Fermin D J, Hao X, Xin H, Schnabel T and Kauk-Kuusik M 2019 Doping and alloying of kesterites *J. Phys.* **1** 044004
[17] Li J, Wang D, Li X, Zeng Y and Zhang Y 2018 Cation substitution in earth-abundant kesterite photovoltaic materials *Adv. Sci.* **5** 1700744
[18] Tseberlidis G, Trifiletti V, Vitiello E, Husien A H, Frioni L, Lisca M D, Alvarez J, Acciarri M and Binetti S O 2022 Band-gap tuning induced by germanium introduction in solution-processed kesterite thin films *ACS Omega* **7** 23445–56
[19] Khadka D B and Kim J 2013 Study of structural and optical properties of kesterite Cu_2ZnGeX_4 (X = S, Se) thin films synthesized by chemical spray pyrolysis *CrystEngComm* **15** 10500–9
[20] Garcia-Llamas E, Merino J M, Serna R, Fontané X, Victorov I A, Pérez-Rodríguez A, León M, Bodnar I V, Izquierdo-Roca V and Caballero R 2016 Wide band-gap tuning $Cu_2ZnSn_{1-x}Ge_xS_4$ single crystals: optical and vibrational properties *Sol. Energy Mater.* **158** 147–53
[21] Trifiletti V, Tseberlidis G, Colombo M, Spinardi A, Luong S, Danilson M, Grossberg M, Fenwick O and Binetti S 2020 Growth and characterization of $Cu_2Zn_{1-x}Fe_xSnS_4$ thin films for photovoltaic applications *Materials* **13** 1471
[22] Chatterjee S and Pal A J 2017 A solution approach to p-type Cu_2FeSnS_4 thin-films and pn-junction solar cells: role of electron selective materials on their performance *Sol. Energy Mater.* **160** 233–40
[23] Donne A L, Trifiletti V and Binetti S 2019 New earth-abundant thin film solar cells based on chalcogenides *Front. Chem.* **7** 297
[24] Chen L, Deng H, Tao J, Cao H, Huang L, Sun L, Yang P and Chu J 2015 Synthesis and characterization of earth-abundant Cu_2MnSnS_4 thin films using a non-toxic solution-based technique *RSC Adv.* **5** 84295–302
[25] Liang X, Guo P, Wang G, Deng R, Pan D and Wei X 2012 Dilute magnetic semiconductor Cu_2MnSnS_4 nanocrystals with a novel zincblende and wurtzite structure *RSC Adv.* **2** 5044–6
[26] Pansuriya T, Malani R and Kheraj V 2022 Investigations on the effect of buffer layer on CMTS based thin film solar cell using SCAPS 1-D *Opt. Mater.* **126** 112150
[27] Arockiadoss K T, Rasu Chettiar A, Linda E and Marasamy L 2024 A cds-free alternative TiS_2 buffer: toward high-performing Cu_2MSnS_4 (M= Co, Mn, Fe, Mg) solar cells *Adv. Theor. Simul.* **8** 2400769
[28] Marchionna S, Donne A L, Merlini M, Binetti S, Acciarri M and Cernuschi F 2017 Growth of Cu_2MnSnS_4 PV absorbers by sulfurization of evaporated precursors *J. Alloys Compd.* **693** 95–102
[29] Donne A L, Marchionna S, Acciarri M, Cernuschi F and Binetti S 2017 Relevant efficiency enhancement of emerging Cu_2MnSnS_4 thin film solar cells by low temperature annealing *Sol. Energy* **149** 125–31
[30] Prabhakar R R, Zhenghua S, Xin Z, Baikie T, Woei L S, Shukla S, Batabyal S K, Gunawan O and Wong L H 2016 Photovoltaic effect in earth abundant solution processed Cu_2MnSnS_4 and $Cu_2MnSn(S,Se)_4$ thin films *Sol. Energy Mater.* **157** 867–73
[31] Yu J, Deng H, Chen L, Tao J, Zhang Q, Guo B, Sun L, Yang P, Zheng X and Chu J 2018 Improvement performance of two-step electrodepositing Cu_2MnSnS_4 thin film solar cells by tuning Cu-Sn alloy layer deposition time *Mater. Chem. Phys.* **211** 382–8
[32] Yu J, Deng H, Zhang Q, Tao J, Sun L, Yang P and Chu J 2018 The role of sulfurization temperature on the morphological, structural and optical properties of electroplated Cu_2MnSnS_4 absorbers for photovoltaics *Mater. Lett.* **233** 111–4
[33] Trifiletti V, Frioni L, Tseberlidis G, Vitiello E, Danilson M, Grossberg M, Acciarri M, Binetti S and Marchionna S 2023 Manganese-substituted kesterite thin-films for earth-abundant photovoltaic applications *Sol. Energy Mater.* **254** 112247
[34] Bhide V G and Dani R H 1961 Electrical conductivity in oxides of manganese and related compounds *Physica* **27** 821–6
[35] Butrichi F, Trifiletti V, Tseberlidis G, Colombo B E G, Taglietti F, Rancan M, Armelao L and Binetti S 2024 Wet synthesis of Cu_2MnSnS_4 thin films for photovoltaics: oxidation control and CdS impact on device performances *Sol. Energy Mater.* **272** 112924

[36] Gobbo C, Di Palma V, Trifiletti V, Malerba C, Valentini M, Matacena I, Daliento S, Binetti S, Acciarri M and Tseberlidis G 2023 Effect of the ZnSnO/AZO interface on the charge extraction in Cd-free kesterite solar cells *Energies* **16** 4137

[37] Turkoglu F, Koseoglu H, Cantas A, Akca F G, Meric E, Buldu D G, Ozdemir M, Tarhan E, Ozyuzer L and Aygun G 2019 Effect of defects and secondary phases in Cu_2ZnSnS_4 absorber material on the performance of Zn (O, S) buffered devices *Thin Solid Films* **670** 6–16

[38] Nie L, Yang J, Yang D and Liu S 2019 Effect of substrate temperature on growth and properties of Cu_2MnSnS_4 thin films prepared by chemical spray pyrolysis *J. Mater. Sci.* **30** 3760–6

[39] Dridi S, Aubry E, Bitri N, Chaabouni F and Briois P 2020 Growth and characterization of Cu_2MnSnS_4 thin films synthesized by spray pyrolysis under air atmosphere *Coatings* **10** 963

[40] Koo H-J 2012 Density functional investigation of the magnetic superstructure of Cu_2MnSnS_4 *Solid State Commun.* **152** 1683–5

[41] Nénert G and Palstra T T M 2009 Magnetoelectric and multiferroic properties of ternary copper chalcogenides $Cu_2MIIMIVS_4$ *J. Condens. Matter Phys.* **21** 176002

[42] Fries T, Shapira Y, Palacio F, Morón M C, McIntyre G J, Kershaw R, Wold A and McNiff E J 1997 Magnetic ordering of the antiferromagnet Cu_2MnSnS_4 from magnetization and neutron-scattering measurements *Phys. Rev. B* **56** 5424–31

[43] Cui Y, Deng R, Wang G and Pan D 2012 A general strategy for synthesis of quaternary semiconductor Cu_2MSnS_4 (M= Co 2+, Fe 2+, Ni 2+, Mn 2+) nanocrystals *J. Mater. Chem.* **22** 23136–40

[44] Behrends J 2010 Spin-dependent transport and recombination in solar cells studied by pulsed electrically detected magnetic resonance (https://doi.org/10.17169/refubium-5249)

[45] Hsiao Y-C, Wu T, Li M and Hu B 2015 Magneto-optical studies on spin-dependent charge recombination and dissociation in perovskite solar cells *Adv. Mater.* **27** 2899–906

[46] Allemand J and Wintenberger M 1970 Propriétés structurales et magnetiques de quelques composes du type stannite *Bulletin de Minéralogie* **93** 14–17

[47] Bernert T and Pfitzner A 2005 $Cu_2MnMIVS_4$ (MIV= Si, Ge, Sn)—analysis of crystal structures and tetrahedra volumes of normal tetrahedral compounds *Z. Kristallogr. Cryst. Mater.* **220** 968–72

[48] Quintero M, Marquina J, Quintero E, Moreno E, Álvarez S, Rincón C, Grima P, Bocaranda P, Rivero D and Henao J A 2014 X-ray diffraction analysis of stannite, wurtz-stannite and pseudo-cubic quaternary compounds by Rietveld method *Rev. Mex. Fis.* **60** 168–75

[49] Alhummiany H 2024 Photoelectrical performance of Cu_2MnSnS_4/p-Si photosensor for solar energy applications *J. Mater. Sci.* **35** 2053

[50] Engberg S, Canulescu S and Schou J 2018 Liquid phase assisted grain growth in Cu_2ZnSnS_4 nanoparticle thin films by alkali element incorporation *RSC Adv.* **8** 7152–8

[51] Bail A L, Duroy H and Fourquet J L 1988 Ab-initio structure determination of $LiSbWO_6$ by x-ray powder diffraction *Mater. Res. Bull.* **23** 447–52

[52] Rodriguez-Carvajal J 2012 FullProfSuite

[53] Thompson P, Cox D E and Hastings J B 1987 Rietveld refinement of Debye–Scherrer synchrotron x-ray data from $Al2O_3$ *J. Appl. Crystallogr.* **20** 79–83

[54] Dedova T *et al* 2025 Sb_2S_3 solar cells with TiO_2 electron transporting layers synthesized by ALD and USP methods *Sol. Energy Mater.* **280** 113279

[55] Rusu M, Kodalle T, Choubrac L, Barreau N, Kaufmann C A, Schlatmann R and Unold T 2021 Electronic structure of the CdS/Cu(In,Ga)Se_2 interface of KF- and RbF-treated samples by Kelvin probe and photoelectron yield spectroscopy *ACS Appl. Mater. Interfaces* **13** 7745–55

[56] Wapler M C, Leupold J, Dragonu I, von Elverfeld D, Zaitsev M and Wallrabe U 2014 Magnetic properties of materials for MR engineering, micro-MR and beyond *J. Magn. Reson.* **242** 233–42

[57] Ren G *et al* 2020 Influences of Cu concentration on electrical properties of CZTSSe absorbers and their device performances *Vacuum* **173** 109121

[58] Xie R, Li Y, Liu H and Zhang X 2017 Insights into the structural, microstructural and physical properties of multiphase powder mixtures *J. Alloys Compd.* **691** 378–87

[59] Balogh L, Ribárik G and Ungár T 2006 Stacking faults and twin boundaries in fcc crystals determined by x-ray diffraction profile analysis *J. Appl. Phys.* **100** 023512

[60] Sławiński W A, Sjåstad A O and Fjellvåg H 2016 Stacking faults and polytypes for layered double hydroxides: what can we learn from simulated and experimental x-ray powder diffraction data? *Inorg. Chem.* **55** 12881–9

[61] Chen X, Wada H, Sato A and Mieno M 1998 Synthesis, electrical conductivity, and crystal structure of $Cu_4Sn_7S_{16}$ and structure refinement of Cu_2SnS_3 *J. Solid State Chem.* **139** 144–51

[62] Idris B, Rafik Z, Kamal D, Abdessalam B and Faouzi G 2015 Size and grain-boundary effects on the performance of polycrystalline CIGS-based solar cells *IREC2015 The Sixth International Renewable Energy Congress* pp 1–5

[63] Sravani L, Routray S, Pradhan K P and Piedrahita M C 2021 Kesterite thin-film solar cell: role of grain boundaries and defects in copper–zinc–tin–sulfide and copper–zinc–tin–selenide *Phys. Status Solidi a* **218** 2100039

[64] Fan P, Lin J, Hu J, Yu Z, Zhao Y, Chen S, Zheng Z, Luo J, Liang G and Su Z 2022 Over 10% efficient Cu_2CdSnS_4 solar cells fabricated from optimized sulfurization *Adv. Funct. Mater.* **32** 2207470

[65] Grossberg M, Salu P, Raudoja J and Krustok J 2013 Microphotoluminescence study of C_2ZnSnS_4 polycrystals *J. Photon. Energy* **3** 30599

[66] Chen R and Persson C 2017 Electronic and optical properties of Cu_2XSnS_4 (X= Be, Mg, Ca, Mn, Fe, and Ni) and the impact of native defect pairs *J. Phys. D: Appl. Phys.* **121** 203104

[67] Grossberg M, Krustok J, Raudoja J and Raadik T 2012 The role of structural properties on deep defect states in Cu_2ZnSnS_4 studied by photoluminescence spectroscopy *Appl. Phys. Lett.* **101** 102102

[68] Afanas′ev V V 2014 Electron band alignment at interfaces of semiconductors with insulating oxides: an internal photoemission study *Adv. Condens. Matter Phys.* **2014** 301302

[69] Koprek A, Cojocaru-Mirédin O, Wuerz R, Freysoldt C, Gault B and Raabe D 2017 Cd and impurity redistribution at the CdS/CIGS interface after annealing of cigs-based solar cells resolved by atom probe tomography *IEEE J. Photovolt.* **7** 313–21

[70] Hwang S K, Park J-H, Cheon K B, Seo S W, Song J E, Park I J, Ji S G, Park M-A and Kim J Y 2020 Improved interfacial properties of electrodeposited $Cu_2ZnSn(S,Se)_4$ thin-film solar cells by a facile post-heat treatment process *Prog. Photovolt.* **28** 1345–54

[71] Poornaprakash B, Amaranatha Reddy D, Murali G, Madhusudhana Rao N, Vijayalakshmi R P and Reddy B K 2013 Composition dependent room temperature ferromagnetism and PL intensity of cobalt doped ZnS nanoparticles *J. Alloys Compd.* **577** 79–85

[72] Hamakawa Y 2013 *Thin-film Solar Cells: Next Generation Photovoltaics and Its Applications* (Springer)
[73] Crovetto A and Hansen O 2017 What is the band alignment of $Cu_2ZnSn(S,Se)_4$ solar cells? *Sol. Energy Mater.* **169** 177–94
[74] Shockley W and Queisser H 2018 Detailed balance limit of efficiency of p–n junction solar cells *Renewable energy* (Routledge) pp Vol2_35–Vol_54
[75] Gobbo C *et al* 2025 Strategies for back contact engineering in high-performance flexible kesterite solar cells *J. Mater. Chem. A Mater.* **13** 25498–508
[76] Tseberlidis G, Di Palma V, Trifiletti V, Frioni L, Valentini M, Malerba C, Mittiga A, Acciarri M and Binetti S O 2023 Titania as buffer layer for Cd-free kesterite solar cells *ACS Mater. Lett.* **5** 219–24
[77] Tseberlidis G, Trifiletti V, Donne A L, Frioni L, Acciarri M and Binetti S 2020 Kesterite solar-cells by drop-casting of inorganic sol–gel inks *Sol. Energy* **208** 532–8
[78] Tseberlidis G, Husien A H, Riva S, Frioni L, Donne A L, Acciarri M and Binetti S 2021 Semi-transparent Cu_2ZnSnS_4 solar cells by drop-casting of sol-gel ink *Sol. Energy* **224** 134–41
[79] Oh J, Kang Y, Seol J H, Kim Y H, Seo J, Lee S U and Ju S-Y 2025 Diffusion and surface effects on sodium-promoted MoS_2 growth observed in operando *Small Methods* **9** e00813
[80] Putthisigamany Y, Rahman K S, Sapeli M M I, Ahmad Ludin N, AdibIbrahim M and Chelvanathan P 2024 Revealing the subtle role of DC-sputtered mo back contact work function in mitigating the detrimental effects of the $MoS_2/MoSe_2$ interfacial layer in kesterite-based thin film solar cells *Energy Fuels* **38** 11188–203
[81] Li S *et al* 2025 Unveiling sodium diffusion kinetics and locking mechanisms for high-performance cztsse photovoltaics *Adv. Sci.* **12** e04087
[82] Bachraoui F E, Tamraoui Y, Louihi S, Alami J, Shahbazian-Yassar R, Yuan Y, Amine K and Manoun B 2021 Unusual superparamagnetic behavior in bulk $Ba_{0.198}La_{0.784}Ti_{0.096}Fe_{0.8O3\mp\delta}$ *Mater. Res. Bull.* **137** 111187
[83] Mezzadri F *et al* 2016 Structural and magnetic characterization of the double perovskite Pb_2FeMoO_6 *J. Mater. Chem. C Mater.* **4** 1533–42
[84] Yuan X, Xu M and Chen Y 2013 Magnetic properties and magnetoresistance effect of Pb_2FeMoO_6 *Appl. Phys. Lett.* **103** 052411
[85] Han J, Yoon J-Y, Ohno H and Fukami S 2025 Unconventional responses in non-collinear antiferromagnets *Newton* **1** 100012
[86] Shukla A, Qian S and Rakheja S 2025 Spintronic devices and applications using noncollinear chiral antiferromagnets *Nanoscale Horiz.* **10** 484–511
[87] Sahoo B C, Jain A, Madaan M, Malik V K and Yusuf S M 2025 Spin canting in the spin-orbit coupled $4d^3$ oxide Ca_3LiRuO_6 *Phys. Rev. B* **112** 54406
[88] Sahlot P and Awasthi A M 2020 Uncompensated-spins induced weak ferromagnetism in $Ca_3Mn_2O_7$: magneto-conductive and dual magneto-capacitive effects *J. Magn. Magn. Mater.* **493** 165732
[89] Hakim M A, Manjurul Haque M, Huq M and Nordblad P 2011 Spin-glass-like ordering in the spinel $ZnFe_2O_4$ ferrite *Phys. Rev. B Condens. Matter* **406** 48–51
[90] Dara H K, Harikrishnan R, Bitla Y, Babu P D 2023 Disorder induced cluster spin glass like state in MnFeSb *J. Magn. Magn. Mater.* **583** 170990
[91] Mydosh J A 2015 Spin glasses: redux: an updated experimental/materials survey *Rep. Prog. Phys.* **78** 052501
[92] Mydosh J A 1993 Spin glasses: an experimental introduction (CRC Press) (https://doi.org/10.1201/9781482295191)
[93] Binder K and Young A P 1986 Spin glasses: experimental facts, theoretical concepts, and open questions *Rev. Mod. Phys.* **58** 801–976
[94] Silva Jr R S, Gainza J, Rodrigues J E, Martínez L, Céspedes E, Nemes N M, Martínez J L and Alonso J A 2022 High-pressure synthesis, spin-glass behaviour, and magnetocaloric effects in $Fe_xTi_2S_4$ heideite sulphides *J. Mater. Chem. C Mater.* **10** 15929–40
[95] Geng Y 2022 Mathematical analysis of Van der Pauw's method for measuring resistivity *J. Phys. Conf. Ser.* **2321** 012027
[96] Kawazu A, Saito Y, Asahi H and Tominaga G 1976 Structure and electrical properties of thin bismuth films *Thin Solid Films* **37** 261–6
[97] Durkaya G 2005 Electrical and structural characterization of bismuth thin films
[98] Yang C 2008 A study of electrical properties in bismuth thin films
[99] Butenko A V, Sandomirsky V, Schlesinger Y, Shvarts D and Sokol V A 1997 Characterization of the electrical properties of semimetallic Bi films by electrical field effect *J. Appl. Phys.* **82** 1266–73
[100] Yánez-Parreño W *et al* 2024 Thin film growth of the Weyl semimetal NbAs *Phys. Rev. Mater.* **8** 34204